Analysis of the Thermal Fisher Information in 2+1 Dimensional Black Hole Spacetimes

by

Everett A. Patterson

A thesis
presented to the University of Waterloo
in fulfillment of the
thesis requirement for the degree of
Master of Science
in
Physics

Waterloo, Ontario, Canada, 2023

Author's Declaration

I hereby declare that I am the sole author of this thesis. This is a true copy of the thesis, including any required final revisions, as accepted by my examiners.

I understand that my thesis may be made electronically available to the public.

Abstract

In the past decade, relativistic quantum information (RQI) has presented itself as a promising avenue for examining the interaction between relativistic and quantum effects. This is most commonly achieved by coupling Unruh-DeWitt detectors to quantum fields in curved spacetime, or by applying quantum properties to otherwise relativistic systems. A lot of attention is placed on what information we can extract from the vacuum state of a quantum field and what can that tell us about the underlying spacetime.

While there has been a lot of theoretical progress made within the field, its experimental applications remain rather scarce. Relativistic quantum metrology (RQM), which concerns itself with the precision of measurements within systems that have both relativistic and quantum effects, is an example of an experimental flavour that RQI can take. One of the metrics of particular importance within RQM is the Fisher information. This form of 'information' quantifies the knowledge that can be extracted about an underlying parameter based on the measurement of a dependent observable parameter.

In this thesis, we consider the thermal Fisher information extracted by a UDW detector in (2+1)-dimensional spacetimes, including the first Fisher information analysis of a black hole spacetime. We provide a detailed analysis of the Fisher information for the BTZ black hole including the identification of the true black hole effects by contrasting our black hole results against those in anti-de Sitter (AdS) spacetime. We further characterize its dependence on various black hole and detector parameters, in addition to describe how the Fisher information might be used as a black hole probe.

We find that the Fisher information is sensitive to the black hole parameters of mass and rotation. So much so in the case of the mass that based on the Fisher information for a given set up, we can identify the mass of the black hole. We also identify novel Fisher information behaviours unique to the BTZ black hole by contrasting these with AdS and previous results (which we actually correct). Beyond acting as a spacetime probe, the Fisher information analysis in this thesis can also enable the improvement of the estimation of the KMS temperature by a UDW detector.

The majority of the work in this thesis can be found on the arXiv in a publicly accessible manuscript [1], and a second manuscript is in progress covering the remainder of the work presented here.

Acknowledgements

There are a great many people who, through roles big and small, have helped shape me into the person and scientist that I am today. While I am a big believer that all small actions have large ripple effects, the people mentioned here are those who have had an indelible impact towards the successful defence of this thesis.

First, I owe a special thanks to my friends and fellow graduate students, Graeme Zinck and Valerie Gilchrist, for their friendships in the early days of my graduate studies, when Covid-19 restrictions made it all but impossible to meet new people let alone spend time with them.

I also want to thank the Waterloo Ultimate community, with special thanks to Devon Asemota, for welcoming me with open arms and providing me with new friends and an outlet for my busy brain to distract itself.

I would like to thank my exceptional supervisor, Robb Mann, for his patience, compassion, support, and encouragement throughout this roller coaster of a degree. Thanks extend to the RBMG for their camaraderie, inspiration, and commiseration. Special thanks to those who have helped me make sense of Mathematica and this whole grad school adventure - notably Erickson, Laura, Ken, Matthew, Jack, and Michael. Special thanks to Haoxing for her help in having me take over her line of research.

I would like to thank my cousin Cameron for giving me "The (Grad School) Talk" during a pit stop on my initial trip to Waterloo from Moncton. Reminding myself of this has helped keep me grounded on more occasions than I can count. And I would like to thank Mike and Jenna for their companionship and commiseration along yet another segment of my academic journey.

Finally, I owe a special thanks to my family for their support and welcoming arms during elongated stays in Moncton as I dodged restrictions and sought comfort.

Dedication

This thesis is dedicated to my Mom, who has been source of both great wisdom and inspiration as I pursue my passion in academia.

Table of Contents

List of Figures

Chapter 1

Introduction

1.1 Motivation and Context

While it is often said that what sets humans apart from other terrestrial lifeforms is their self-awareness, this deep-seated curiosity extends well beyond oneself. For millennia, humans have sought to understand and explain the strange universe which we inhabit. While there are written accounts dating as far back as the Greco-Roman period addressing questions about the fundamental components of nature and the far-flung reaches of the cosmos, our understanding of the very big and very small components of our universe have grown through the ages as rigorous science and physics became increasingly developed.

As with many things, this progress has compounded on itself over the years leading to rapid growth since the renaissance. And while our understanding of the world around us has never been as complete as it is today, neither have we been so aware of the shortcomings of our theories.

Two of the most successful physical theories of the 20th century are that of quantum mechanics and of general relativity. Developed in the early part of the 20th century to address long standing issues within previous classical theories, these two theories effectively revolutionized the field of physics setting the stage for much of the research that is done today.

Some might peg the year 1905 as the start of this revolution during Einstein's Annus Mirabilis which set the stage for quantum and relativity with the explanation of the photoelectric effect and the description of special relativity. A decade later, Einstein proposed the more complete theory of general relativity, which at its core describes gravity as being

the curvature of spacetime. In addition to this new gravitational perspective, relativity redefined our understanding of time and simultaneity to being observer-dependent, rather than a fixed global property of our universe [2].

Meanwhile, in the 1920s, Schroedinger and Heisenberg indepedently developed equivalent theories of quantum mechanics. Schroedinger's picture describes the time evolution of quantum states acted upon by time-independent operators, while Heinsenberg's picture describes a stationary state that is acted upon by time-dependent operators. Besides the idea of energy being discrete rather than continuous, quantum theory also ushered a shift from deterministic to probabilistic theories [3].

Quantum mechanics has since led to quantum field theory (QFT) and the Standard Model which effectively describe all non-gravitational physics. In particular, QFT does successfully incorporate special relativity with quantum mechanics by describing particles as excitations of their underlying quantum field. And while there remain a lot of questions that are not answered by QFT, within its regime of validity it is a remarkably successful theory. The most notable example of this is quantum electrodynamics (QED), in which the experimentally determined anomalous magnetic dipole moment of the electron agrees with the calculations to nine orders of precision [4].

Likewise, there have been many developments in the field of relativity in the past century. These include higher curvature theories, gravitational waves, and black holes, with the latter two leading to Nobel and Breakthrough Prizes in the last decade [5, 6, 7, 8].

However, for all their success, quantum mechanics and general relativity are fundamentally at odds with each other. Quantum mechanics is a probabilistic theory with inescapable uncertainty which best describes small-scale systems. Whereas general relativity is a deterministic theory that addresses either very massive (and often large) systems and those that move at high velocities. There have been many attempts to reconcile these juggernauts of modern physics [9], though two of the most recent paradigms (string [10] and loop theories [11]) have seemingly stalled.

In their wake a new approach towards a theory of quantum gravity has emerged in Relativistic Quantum Information (RQI) [12], which seeks to consider both the effects of relativity on quantum information protocols and how quantum information tools can help us describe and probe relativistic systems. RQI relies heavily on QFT in curved space [13], and while not claiming to be a full theory of quantum gravity, it does allow for the interaction between quantum and relativistic effects in new and instructive ways. One of the best probes for such interactions is the two-level quantum detector called Unruh-DeWitt (UDW) detector [14, 15]. Locally coupling these UDW detectors to the quantum vacuum that permeates space allows us to glean insight into the structure of spacetime by

comparing the behaviour of the detector in different spacetimes. In particular, there has been significant interest within the field to try to extract information from the quantum vacuum using UDW detectors through methods such as entanglement harvesting [16, 17].

There is also the sub-field of Relativistic Quantum Metrology (RQM) which ostensibly concerns itself with the precision of measurements within systems that have both relativistic and quantum contributions [18, 19]. While standard quantum metrology has been around for some time now [20, 21, 22], incorporating relativistic effects is a more recent development. RQM is not only crucial to the experimental implementation of many new quantum technologies, it also offers a new theoretical perspective into the interaction between the quantum and relativistic theories [23, 24, 25].

Previous work along this vein has used a measure called the Fisher information (FI) as a framework to infer information about the spacetime's underlying structure. This approach has been used to estimate the expansion rate of the universe [18, 26], to explore time dilation of quantum clocks [27, 28] and the Unruh effect [29], and to make progress towards quantum communication technologies [30]. More recently, UDW detectors and FI applied to a thermal parameter has been used to uncover structure within de Sitter (dS) and anti-de Sitter (AdS) spacetimes in 3+1 dimensions [31].

In this thesis, we are interested in probing the intersection of relativistic and quantum theories. To do this, we will apply tools from RQI and RQM to the task of probing black holes, which owing to their small size and large mass are widely seen as a possible window into relativistic quantum effects. In particular, we will consider the thermal Fisher information extracted from the vacuum state of black hole spacetimes in 2+1 dimensions via UDW detectors.

1.2   Outline

This thesis is organized as follows. In Chapter 2, we will present the theoretical framework upon which the work is done. This will include an introduction to the Fisher information, to UDW detectors, and to the spacetimes under consideration.

Having done this, we will present the derivations that were required to obtain our results in Chapter 3. This chapter covers the high-level steps of the response rate derivations, while the details are left to Appendix A. It is also here that we will outline our estimation protocol.

Next, we will proceed to Chapter 4, where we present our analysis of the Fisher information in black hole spacetimes. This Chapter features many insightful plots to assist in

our description of the Fisher information and its behaviours.

Finally, we will conclude in Chapter 5 with a summary of the work contained in this thesis followed by future directions.

Chapter 2

Theory

Before we delve into the results and derivations of this paper, let us first present the theoretical foundations of this work.

2.1 Fisher information

A crucial element of the scientific method is the ability to test a theory or a hypothesis against real-world evidence. This back-and-forth between theorists and experimentalists dates back to the very inception of the scientific method, with many of its pioneers donning both hats. These early scientists sought to test the theories they developed with experimental set ups while also explaining what they observed in the world around them with powerful theories.

While many theorists do have an interest in experiments and vice versa, the last century has seen the discipline branch into two increasingly distinct fields of theoretical and experimental physics. The motivations for both lie in the realm of the other, but the challenges within each separate field are such that scientists tend to specialize in order to be able to contribute to new and exciting results.

Once upon a time, it was sufficient to take a ruler and measure the distance travelled by a moving object, or to use a stopwatch to record the time elapsed between two events. Notwithstanding the relativistic effects that are present in certain systems, we were able to measure pretty much anything we wanted using an appropriately calibrated instrument associated to a well-defined unit for the quantity being measured. Even the once-popular liquid mercury thermometers fit this model.

However, at the frontiers of physics, where we seek to measure very minute effects with great confidence, we require more than tangible tools. Once we have optimized our measurement device to reduce the systematic errors, we are able to further improve the accuracy and precision of our results by applying statistical tools to the raw data.

Great examples of this in contemporary physics are the Canadian Hydrogen Intensity Mapping Experiment (CHIME) which is radio telescope designed for the detection of fast radio bursts, pulsars, and eventually the expansion of the Universe via hydrogen mapping [32] and the Event Horizon Telescope (EHT) which makes use of eight telescopes located in six different places across the globe to effectively serve as a single telescope with an Earth-sized aperture [8]. Both of these use relatively simple physical telescopes enhanced by exceptional data analysis to produce meaningful results, not evident from the naked data.

In particular, there are times when the value we seek to observe is not directly visible to us. This is not uncommon in quantum mechanics, where not every parameter of interest corresponds to a quantum observable. In these cases we must exploit correlations between underlying unknown parameters and observable parameters. The most popular way of quantifying this correlation is by making use of what is known as the Fisher information. This sort of information rigorously quantifies the knowledge of an underlying parameter that can be estimated from the measurement of a dependent observable parameter.

Suppose an observable parameter $x \in X$ has a dependence on an underlying parameter $\xi \in \Xi$ that is characterized by the probability distribution $p(x|\xi)$, where (X, Ξ) represents the set of possible observable and underlying parameters respectively.

If $\hat{\xi}$ is the estimator, $\hat{\xi} : X^n \to \Xi$, which given a sample of n observed parameters x returns the underlying parameter ξ, and this estimator is unbiased (i.e., it returns the actual value of ξ), then the Fisher information, $\mathcal{I}(\xi)$, is defined to be

$$\mathcal{I}(\xi) = \int p(x|\xi) \left(\frac{\partial \ln p(x|\xi)}{\partial \xi} \right)^2 dx = \int \frac{1}{p(x|\xi)} \left(\frac{\partial p(x|\xi)}{\partial \xi} \right)^2 dx. \qquad (2.1)$$

This is an integral(sum) over all possible observable values, weighted by the probability distribution $p(x|\xi)$, of the square of the logarithmic derivative of this probability with respect to the underlying parameter.

The primary value of the Fisher information to most experimentalists arises from a property stating that it provides a lower bound on the possible variance of the estimator. In particular, the Cramér-Rao bound [33, 34]

$$\mathrm{var}(\hat{\xi}) \geq \frac{1}{n\mathcal{I}(\xi)}, \qquad (2.2)$$

imposes a lower bound on the variance of the estimator that is inversely proportional to the Fisher information. Thus, if we have little Fisher information, the lower bound on the variance of the estimator will be large, limiting our ability to extract the desired information about the underlying parameter. Conversely, if the Fisher information is large, then its inverse is small, which results in a smaller lower bound on the variance. This means that there exists some estimator that can better predict the value of the underlying variable.

We note that number of observable parameter measurements, n, is also inversely proportional to the theoretically optimal variance. This is not surprising as we might expect that the more measurements that are applied, the more 'information' we can gather; though we note that n does not contribute to our definition of Fisher information, but rather comes into play in its application to the Cramer-Rao bound.

2.2 Unruh-DeWitt detectors

Quantum field theory is a language that we can use to describe all things quantum. In this theory, quantum fields permeate spacetime and excitations within the field correspond to particles in emergent theories. While the definition of a particle can become somewhat murky in these waters, we will adhere to Unruh's maxim that "a particle is what a particle detector detect" [35]. Such systems can be used to extract information about the global state of the quantum field by measuring a particle detector that is locally coupled to the field.

Among such detectors, the most prevalent in the literature today is the Unruh-De Witt (UDW) particle detector, which is a simple two-level quantum system that effectively models the light matter interaction without exchange of angular momentum. This model has seen widespread use in entanglement harvesting [17, 36, 16], as well as the detection of novel effects such as the anti-Unruh effect [37, 38].

The ground state, $|0_D\rangle$, and excited state, $|1_D\rangle$, of our detector are separated by some energy gap, Ω. The proper time of the detector, τ, is used to parameterize its trajectory, $x(\tau)$. The detector is coupled to a massless scalar field with the coupling described by the interaction Hamiltonian

$$H_I = \lambda\chi(\tau)\left(e^{i\Omega\tau}\sigma^+ + e^{-i\Omega\tau}\sigma^-\right) \otimes \phi[x(\tau)], \tag{2.3}$$

where λ is the coupling constant, $\sigma^+ = |1_D\rangle\langle 0_D|$ and $\sigma^- = |0_D\rangle\langle 1_D|$ are ladder operators.

Working in the perturbative regime, where the coupling constant, λ, is small, we can define the response function, F (related to the transition probability), which quantifies

the likelihood of the detector being found in the excited or ground state. This response function can be expressed as

$$F(\Omega) = \int_{-\infty}^{\infty} d\tau \int_{-\infty}^{\infty} d\tau' \, e^{-i\Omega(\tau-\tau')} \, W(x(\tau), x(\tau')), \qquad (2.4)$$

where $W(x(\tau), x(\tau'))$ is the Wightman function. The Wightman function, which is dependent on the underlying spacetime, quantifies the correlation between two points x and x' within the field parameterized by the proper time of the detector at those points. This function, sometimes aptly referred to as the two-point correlation function is given by

$$W(x(\tau), x(\tau')) = \langle 0 | \, \hat{\phi}(x(\tau)) \hat{\phi}(x(\tau')) \, | 0 \rangle \,. \qquad (2.5)$$

In the special case that our detector is on a stationary trajectory (i.e., one that has fixed spatial coordinates, but changing time coordinate), then the Wightman function is entirely defined by the change in time $\Delta\tau = \tau' - \tau$. Given such a trajectory, we are capable of defining the response per unit time, also called the response rate [39, 40]. This can be thought of as the derivative of the response function with respect to time and is given by

$$\mathcal{F}(\Omega) = \int_{-\infty}^{\infty} d\Delta\tau \, e^{-i\Omega\Delta\tau} \, W(\Delta\tau). \qquad (2.6)$$

This response rate has important applications to UDW detectors in open quantum system frameworks.

We will be specifically interested in the ability of a UDW detector to measure the temperature of the spacetime and its ability to discriminate between spacetimes [41, 42, 43, 44, 45]. We observe thermal states in expanding dS spacetime [13, 46], for uniform detector acceleration, or more generally whenever there is an event horizon [47]. It is well known that a UDW detector near a black hole will experience thermal radiation [48], but it is also the case that such a detector will experience thermal radiation in AdS provided that it has a sufficiently large acceleration [49, 50]. As such it is clear that thermal states are an important part of a given spacetime.

2.3 Spacetimes

While we ultimately want to consider what the thermal Fisher information of a UDW detector can tell us about black hole spacetimes, it will be useful for us to first consider

this Fisher information for a constantly accelerating detector in AdS spacetime. Not only will the AdS spacetime allow us to produce a quotient space construction of our black hole spacetime using an image sum, but it will also provide a non-black hole spacetime against which to compare our new results.

By considering (2+1)-dimensional spacetime, we will be able to construct the simple BTZ black hole solutions to Einstein equations via AdS$_3$.

2.3.1   AdS-Rindler

Anti-de Sitter space is the simplest maximally symmetric solution to the Einstein equations that has constant negative spacetime curvature (equivalent to a negative cosmological constant). In (2+1)-dimensional spacetime, AdS with cosmological constant $\Lambda = -1/\ell^2$, where $\ell > 0$ is known as the AdS length, can be expressed as the hyperboloid

$$X_1^2 + X_2^2 - T_1^2 - T_2^2 = -\ell^2, \tag{2.7}$$

embedded in $(2+2)$-dimensional flat spacetime with 'position' coordinates X_1, X_2, 'time' coordinates T_1, T_2, and the metric

$$ds^2 = dX_1^2 + dX_2^2 - dT_1^2 - dT_2^2. \tag{2.8}$$

Since we will be specifically interested in detectors that can thermalize, we require that our detector trajectories have super-critical constant acceleration, $a \geq 1/\ell$ [39]. When working with constantly accelerating trajectories in AdS, one can opt to work in what are known as Rindler coordinates.

We can thus make our lives easier by working with the AdS-Rindler metric

$$ds^2 = -\left(\frac{r^2}{\ell^2} - 1\right) dt^2 + \left(\frac{r^2}{\ell^2} - 1\right)^{-1} dr^2 + r^2 d\phi^2, \tag{2.9}$$

which can be obtained from the standard AdS metric by applying the coordinate transformations

$$\begin{aligned}
T_1 &= \ell\sqrt{\frac{r^2}{\ell^2}} \cosh\phi\,, \quad X_1 = \ell\sqrt{\frac{r^2}{\ell^2}} \sinh\phi\,, \\
T_2 &= \ell\sqrt{\frac{r^2}{\ell^2} - 1} \sinh\frac{t}{\ell}\,, \quad X_2 = \ell\sqrt{\frac{r^2}{\ell^2} - 1} \cosh\frac{t}{\ell}\,,
\end{aligned} \tag{2.10}$$

where the time parameter, t, can take on any real value, the radial parameter, r, must be a non-negative real number, the ϕ parameter is also free to take any real value, and ℓ is the AdS length. Note that when $r = \ell$ we encounter an acceleration horizon.

The Wightman function (for a conformally coupled massless scalar field) in (2+1)-dimensional AdS [51, 52] is given by

$$W_{\text{AdS}}(x, x') = \frac{1}{4\pi\sqrt{2}\ell} \left(\frac{1}{\sqrt{\sigma(x, x')}} - \frac{\zeta}{\sqrt{\sigma(x, x') + 2}} \right), \tag{2.11}$$

where

$$\sigma(x, x') = \frac{1}{2\ell^2} \left[(X_1 - X_1')^2 - (T_1 - T_1')^2 + (X_2 - X_2')^2 - (T_2 - T_2')^2 \right], \tag{2.12}$$

is the squared geodesic distance between the points x and x'. The parameter $\zeta \in \{0, 1, -1\}$ specifies the boundary conditions to be satisfied at spatial infinity, with its possible values corresponding to what are commonly referred to as the transparent ($\zeta = 0$), Dirichlet ($\zeta = 1$), and Neumann ($\zeta = -1$) boundary conditions.

In AdS-Rindler, the squared distance can be shown to be

$$\sigma(x, x') = -1 + \frac{rr'}{\ell^2} \cosh(\Delta\phi) - \frac{\sqrt{(r^2 - \ell^2)(r'^2 - \ell^2)}}{\ell^2} \cosh\left(\frac{\Delta t}{\ell}\right), \tag{2.13}$$

where $\Delta\phi = \phi - \phi'$ and $\Delta t = t - t'$. Details for this calculation can be found in Appendix A.

2.3.2 Static BTZ Black Hole

Starting from the hyperboloid embedding described in the previous section, we can obtain the static BTZ black hole metric

$$ds^2 = -\left(\frac{r^2}{\ell^2} - M\right) dt^2 + \left(\frac{r^2}{\ell^2} - M\right)^{-1} dr^2 + r^2 d\phi^2, \tag{2.14}$$

by applying the following transformations

$$T_1 = \ell\sqrt{\frac{r^2}{M\ell^2}} \cosh(\sqrt{M}\phi), \quad X_1 = \ell\sqrt{\frac{r^2}{M\ell^2}} \sinh(\sqrt{M}\phi),$$

$$T_2 = \ell\sqrt{\frac{r^2}{M\ell^2} - 1} \sinh\frac{\sqrt{M}t}{\ell}, \quad X_2 = \ell\sqrt{\frac{r^2}{M\ell^2} - 1} \cosh\frac{\sqrt{M}t}{\ell}. \tag{2.15}$$

followed by the identification $\Gamma : \phi \to \phi + 2\pi$.

Noting the similarities between these transformations and those from the section above, we can obtain the BTZ Wightman function for the Hartle-Hawking vacuum from the AdS Wightman function by using the method of images [53]:

$$W_{\text{BTZ}}(x, x') = \sum_{n=-\infty}^{\infty} W_{\text{AdS}}(x, \Gamma^n x') \tag{2.16}$$

where $W_{\text{AdS}}(x, x')$ is the vacuum Wightman function defined in Equation (2.11) associated with a massless conformally coupled scalar field, and $\Gamma^n x'$ denotes the action of the identification on the spacetime point x'.

Applying Equations (2.11) and (2.12), this works out to be

$$W_{\text{BTZ}}(x, x') = \frac{1}{4\pi\sqrt{2}\ell} \sum_{n=-\infty}^{\infty} \left[\frac{1}{\sqrt{\sigma_n}} - \frac{\zeta}{\sqrt{\sigma_n + 2}} \right], \tag{2.17}$$

where

$$\sigma_n(x, x') := -1 + \frac{rr'}{r_{\text{h}}^2} \cosh\left[\frac{r_{\text{h}}}{\ell}(\Delta\phi - 2\pi n)\right] - \frac{\sqrt{(r^2 - r_{\text{h}}^2)(r'^2 - r_{\text{h}}^2)}}{r_{\text{h}}^2} \cosh\left[\frac{r_{\text{h}}}{\ell^2}\Delta t\right]. \tag{2.18}$$

Note that the black hole radius, r_h, is related to the black hole mass by $r_h = \sqrt{M}\ell$. We will express all of our final results in terms of the mass, but we perform a number of our derivations in terms of the radius.

2.3.3 Rotating BTZ Black Hole

Our approach to characterizing the rotating counterpart of our (2+1)-dimensional black hole spacetime is more direct.

The line element of the rotating BTZ black hole in "Schwarzschild" coordinates [54, 51] is given by

$$ds^2 = -\left(N^\perp\right)^2 dt^2 + f^{-2}dr^2 + \left(d\phi + N^\phi dt\right)^2, \tag{2.19}$$

where, $N^\perp = f = \sqrt{-M + \frac{r^2}{\ell^2} + \frac{J^2}{4r^2}}$ and $N^\phi = -\frac{J}{2r^2}$, with $M = \frac{r_+^2 + r_-^2}{\ell^2}$, the mass of the black hole, and $J = \frac{2r_+ r_-}{\ell}$, the angular momentum of the black hole. The inner and outer radii are r_- and r_+, while ℓ remains the AdS length.

It is worth noting that $|J| \leq M\ell$, with equality corresponding to extremal rotation, when $r_+ = r_-$. Further note that if $J = 0$ (or equivalently $r_- = 0$), then we are indeed left with the static BTZ spacetime with $r_+ = r_{\mathrm{h}}$.

While we will use the mass M and angular momentum J to ultimately describe the black hole, our algebraic manipulations will be performed in terms of $r_\pm$, where

$$r_\pm^2 = \frac{M\ell}{2}\left[1 \pm \sqrt{1 - \left(\frac{J}{M\ell}\right)}\right]. \tag{2.20}$$

The metric can be expressed in terms of these radii by substituting them directly into Equation (2.19). Alternatively, it can also be obtained from the embedded hyperboloid of Equation (2.7) and the associated metric from Equation (2.8) via the transformations

$$T_1 = \ell\sqrt{\alpha}\cosh\left(\frac{r_+}{\ell}\phi - \frac{r_-}{\ell^2}t\right), \quad X_1 = \ell\sqrt{\alpha}\sinh\left(\frac{r_+}{\ell}\phi - \frac{r_-}{\ell^2}t\right),$$
$$T_2 = \ell\sqrt{\alpha - 1}\cosh\left(\frac{r_+}{\ell^2}t - \frac{r_-}{\ell}\phi\right), \quad X_2 = \ell\sqrt{\alpha - 1}\cosh\left(\frac{r_+}{\ell^2}t - \frac{r_-}{\ell}\phi\right). \tag{2.21}$$

followed by the identification $\Gamma : \phi \to \phi + 2\pi$, and where

$$\alpha(r) = \frac{r^2 - r_-^2}{r_+^2 - r_-^2}. \tag{2.22}$$

The form of the Wightman function for the rotating and static BTZ spacetimes has the same general form

$$W_{\mathrm{BTZ}}(x, x') = \frac{1}{4\pi\sqrt{2}\ell}\sum_{n=-\infty}^{\infty}\left[\frac{1}{\sqrt{\sigma_n}} - \frac{\zeta}{\sqrt{\sigma_n + 2}}\right], \tag{2.23}$$

although the squared distance is slightly more involved owing to the presence of the inner radius r_- [52]. It is thus given by

$$\sigma_n(x, x') = -1 + \sqrt{\alpha(r)\alpha(r')}\cosh\left[\frac{r_+}{\ell}(\Delta\phi - 2\pi n) - \frac{r_-}{\ell^2}(\Delta t)\right]$$
$$- \sqrt{(\alpha(r) - 1)(\alpha(r') - 1)}\cosh\left[\frac{r_+}{\ell^2}(\Delta t) - \frac{r_-}{\ell}(\Delta\phi - 2\pi n)\right], \tag{2.24}$$

where $\Delta t = t - t'$ and $\Delta\phi = \phi - \phi'$.

Chapter 3

Derivations

In this chapter, we will be presenting the specific systems, with particular detector and spacetime set ups, that we will be examining in this thesis and some of the key steps towards obtaining these results.

3.1   Computing Response Rates

In order to compute the response rate of our detector, which we will eventually require to compute the Fisher information, it is important that we specify the trajectory along which the detector will be travelling.

Within each spacetime under consideration, namely AdS, the static BTZ black hole, and the rotating BTZ black hole, there are a number of possible detector trajectories that each possess particular behaviours. These trajectories can often be characterized by their symmetries, which in turn can help provide a better intuition into the structure of the spacetime.

Since we are looking to elicit a thermal response in our detector, we limit ourselves detectors in AdS with super-critical accelerations, $a > 1/\ell$. This corresponds to a stationary detector in the coordinates of the previously defined AdS-Rindler spacetime.

In the case of the static BTZ black hole, we will also choose a stationary trajectory for our detector. In addition to being the simplest trajectory that we can choose, the stationary trajectory will mimic the experience of the constantly accelerating detector in AdS. This will allow us to compare and contrast the two spacetimes in order to identify what behaviours can truly be attributed to the black hole nature of the BTZ spacetime.

Finally, for the rotating BTZ black hole, we will consider our detector to be moving along a co-rotating trajectory. That is to say, our detector will rotate about the black hole with the same angular velocity as the black hole itself. This trajectory similarly mimics the stationary detector and static black hole combination, allowing us to isolate the rotational contributions to the Fisher information.

3.1.1 Accelerated detector in AdS

A constantly accelerating detector in AdS is represented as a stationary detector in AdS-Rindler. Such a detector has a trajectory defined by

$$x_D(\tau) := \{t = \frac{\tau}{\sqrt{f(R_D)}}, \, r = R_D, \, \phi = \Phi_D\}, \tag{3.1}$$

where the proper time of the detector, τ, can be related to the coordinate time by the red-shift factor $\gamma_D = \frac{d\tau}{dt} = \sqrt{f(R_D)}$, where $f(r) = r^2/\ell^2 - 1$. This trajectory is dubbed stationary because the detector remains at a fixed radial and angular position. Thus the only motion is forward in time.

Recall that to compute the response rate, we require the Wighman function, which in turn requires us to first compute the squared geodesic distance, $\sigma(x, x')$, between two points x and x' along our trajectory.

We begin substituting the stationary trajectory coordinates into Equation (2.13)'s definition of the squared distance. Noting that $r = r' = R_D$ and $\phi = \phi' = \Phi_D$, we find that

$$\sigma(x, x') = -2f(R_D) \sinh^2\left(\frac{\Delta\tau}{2\ell\sqrt{f(R_D)}}\right). \tag{3.2}$$

Plugging this into the AdS Wightman function from Equation (2.11), we get that

$$W_{\text{AdS}}(x, x') = \frac{1}{8\pi\ell\sqrt{f(R_D)}} \left(\frac{1}{\sqrt{-\sinh^2(\Delta\tau/(2\sqrt{f(R_D)}\ell))}} \right.$$

$$\left. - \frac{\zeta}{\sqrt{1/f(R_D) - \sinh^2(\Delta\tau/(2\sqrt{f(R_D)}\ell))}} \right) \tag{3.3}$$

$$= \frac{T}{4} \left(\frac{1}{\sqrt{-\sinh^2(\Delta\tau\pi T)}} - \frac{\zeta}{\sqrt{4\pi^2\ell^2 T^2 - \sinh^2(\Delta\tau\pi T)}} \right), \tag{3.4}$$

where we have made use of the relation between the KMS temperature, T, and the radial position of the detector, R_D,

$$T = \frac{\sqrt{a^2\ell^2 - 1}}{2\pi\ell} = \frac{1}{2\pi\ell}\frac{1}{\sqrt{f(R_D)}}, \tag{3.5}$$

where the inverse KMS temperature, $\beta = 1/T$, is defined to be the imaginary period of the Wightman function for a field satisfying the KMS [55, 56] condition

$$W(\tau - i\beta, \tau') = W(\tau', \tau). \tag{3.6}$$

Finally, to compute the response rate from Equation (2.6) with this Wightman function, we find that the response rate of a uniformly accelerating detector in $(2 + 1)$-dimensional AdS is [50]

$$\mathcal{F}_{\text{AdS}} = \frac{1}{4} - \frac{i}{4\pi}\text{PV}\int_{-\infty}^{\infty} dz \frac{e^{-i\Omega z/(\pi T)}}{\sinh z} - \frac{\zeta}{2\pi\sqrt{2}}\text{Re}\int_{0}^{\infty} dz \frac{e^{-i\Omega z/(2\pi T)}}{\sqrt{1 + 8\pi^2\ell^2 T^2 - \cosh z}}, \tag{3.7}$$

where we applied the substitution $z = \pi T\Delta\tau$, PV is the Cauchy principle value, and Re represents the real part. A more detailed derivation can be found in Appendix A, though this result can also be obtained by dividing the infinite interaction time limit of the response function by $\sqrt{\pi}$.

Performing the integrals, we find that the response rate can be explicitly written as

$$\mathcal{F}_{\text{AdS}} = \frac{1}{4}\left[1 - \tanh\left(\frac{\Omega}{2T}\right)\right] \times \left\{1 - \zeta P_{-\frac{1}{2}+\frac{i\Omega}{2\pi T}}\left(1 + 8\pi^2\ell^2 T^2\right)\right\}, \tag{3.8}$$

where P_ν is the associated Legendre function of the first kind, satisfying $P_{-1/2+i\lambda} = P_{-1/2-i\lambda}$.

3.1.2 Stationary detector in static BTZ

Much like the stationary detector in AdS-Rindler, the trajectory of a stationary detector in BTZ spacetime can be parametrized by

$$x_D(\tau) := \{t = \tau/\gamma_D,\ r = R_D,\ \phi = \Phi_D\}, \tag{3.9}$$

where the proper time of the director, τ, is related to the coordinate time, t, by the red-shift factor of

$$\gamma_D = \sqrt{\frac{R_D^2}{\ell^2} - M}. \tag{3.10}$$

Sometimes this redshift factor is expressed in terms of the black hole radius, $r_h = \sqrt{M}\ell$, rather than the black hole mass.

Given the stationary trajectory of our detector, we can update the squared distance formula from Equation (2.18) to be expressed as

$$\sigma_n(x, x') = -1 + (\frac{\gamma_D^2}{M} + 1)\cosh\left[2\pi n\sqrt{M}\right] - \frac{\gamma_D^2}{M}\cosh\left[\frac{\sqrt{M}\Delta\tau}{\gamma_D\ell}\right], \tag{3.11}$$

which then allows us to rewrite the BTZ Wightman function from Equation (2.17) in the specific case of our trajectory as

$$W_{\text{BTZ}}(x, x') = \frac{1}{4\sqrt{2}\pi\ell} \sum_{n=-\infty}^{\infty} \left[\frac{1}{\sqrt{-1 + (\frac{\gamma_D^2}{M} + 1)\cosh\left[2\pi n\sqrt{M}\right] - \frac{\gamma_D^2}{M}\cosh\left[\frac{\sqrt{M}\Delta\tau}{\gamma_D\ell}\right]}} \right.$$

$$\left. - \frac{\zeta}{\sqrt{1 + (\frac{\gamma_D^2}{M} + 1)\cosh\left[2\pi n\sqrt{M}\right] - \frac{\gamma_D^2}{M}\cosh\left[\frac{\sqrt{M}\Delta\tau}{\gamma_D\ell}\right]}} \right] \tag{3.12}$$

$$= \frac{T}{2\sqrt{2}} \sum_{n=-\infty}^{\infty} \left[\frac{1}{\sqrt{\alpha_n^- - \cosh[2\pi T\Delta\tau]}} - \frac{\zeta}{\sqrt{\alpha_n^+ - \cosh[2\pi T\Delta\tau]}} \right], \tag{3.13}$$

where

$$\alpha_n^{\pm} = \pm 4\pi^2\ell^2 T^2 + (1 + 4\pi^2\ell^2 T^2)\cosh\left[2\pi n\sqrt{M}\right]. \tag{3.14}$$

16

The KMS temperature at a radius R_D from the BTZ black hole has a very similar expression to that of AdS, except that in addition to the redshift factor there is also some mass dependence as seen in

$$T = \frac{1}{2\pi\ell} \frac{\sqrt{M}}{\gamma_D}. \tag{3.15}$$

Having found a trajectory-specific description for the Wightman function, we are now in a position to compute the response rate from Equation (2.6) for our stationary detector in BTZ spacetime. Applying the substitution $z = 2\pi T \Delta\tau$, we obtain

$$\mathcal{F}_{\text{BTZ}} = \mathcal{F}_{\text{AdS}} + \frac{1}{\sqrt{2\pi}} \sum_{n=1}^{\infty} \left\{ \int_0^{\infty} dz \ \text{Re} \left[\frac{\exp\left(-i\Omega z/(2\pi T)\right)}{\sqrt{\alpha_n^- - \cosh(z)}} \right] \right.$$
$$\left. - \zeta \int_0^{\infty} dz \ \text{Re} \left[\frac{\exp\left(-i\Omega z/(2\pi T)\right)}{\sqrt{\alpha_n^+ - \cosh(z)}} \right] \right\}. \tag{3.16}$$

Computing the integrals, we can compactly write the response rate as

$$\mathcal{F}_{\text{BTZ}} = \frac{1}{4} \left[1 - \tanh\left(\frac{\Omega}{2T}\right) \right] \sum_{n=-\infty}^{n=\infty} \left[P_{-\frac{1}{2}+\frac{i\Omega}{2\pi T}}\left(\alpha_n^-\right) - \zeta P_{-\frac{1}{2}+\frac{i\Omega}{2\pi T}}\left(\alpha_n^+\right) \right]. \tag{3.17}$$

Note that we recover the AdS response rate when we restrict ourselves to the n=0 term.

3.1.3 Co-rotating detector in rotating BTZ

For the rotating BTZ spacetime, we will choose to have our detector follow a co-rotating trajectory. This trajectory, for which we can imagine our detector orbiting the black hole with the same angular velocity in the plane of motion, can be parameterized by

$$x_D(\tau) := \{t = \ell\tau/\gamma_D, \ r = R_D, \ \phi = r_-\tau/(r_+\gamma_D)\}, \tag{3.18}$$

where r_- and r_+ are the inner and outer radii of the black hole.

In the co-rotating frame, the redshift factor is $\gamma_D = \sqrt{(r^2 - r_+^2)(r_+^2 - r_-^2)}/r_+$. We thus have

$$t = \frac{\ell\tau}{\gamma_D} = \frac{\ell r_+ \tau}{\sqrt{(r^2 - r_+^2)(r_+^2 - r_-^2)}} \tag{3.19}$$

and

$$\phi = \frac{r_-}{r_+} \frac{\tau}{\gamma_D} = \frac{r_-\tau}{\sqrt{(r^2 - r_+^2)(r_+^2 - r_-^2)}}. \tag{3.20}$$

We can thus relate the angular and time coordinates by $\phi = \frac{r_-}{\ell r_+}t$ and express the squared geodesic distance from Equation (2.24) along our particular trajectory as

$$\sigma_n(x, x') = -1 + \alpha(R_D) \cosh\left[\frac{2\pi n r_+}{\ell}\right] - (\alpha(R_D) - 1)\cosh\left[\frac{2\pi n r_-}{\ell} + \frac{\Delta\tau}{\sqrt{\alpha(R_D) - 1}\ell}\right], \tag{3.21}$$

where $\alpha(r) = \frac{r^2 - r_-^2}{r_+^2 - r_-^2}$.

Making use of the KMS temperature's relation to the radius of the detector's trajectory,

$$T = \frac{1}{2\pi\ell}\sqrt{\alpha(R_D) - 1}, \tag{3.22}$$

we can rewrite any expression in R_D in terms of T via $\alpha(R_D) - 1 = (4\pi^2 T^2 \ell^2)^{-1}$. Doing so and plugging the resulting squared distance into the Wightman function formula, we obtain

$$W_{\mathrm{RBTZ}}(x, x') = \frac{T}{2\sqrt{2}} \sum_{n=-\infty}^{\infty} \left[\frac{1}{\sqrt{\alpha_n^- - \cosh\left[\frac{2\pi n r_-}{\ell} + 2\pi T \Delta\tau\right]}} - \frac{\zeta}{\sqrt{\alpha_n^+ - \cosh\left[\frac{2\pi n r_-}{\ell} + 2\pi T \Delta\tau\right]}}\right], \tag{3.23}$$

where

$$\alpha_n^\pm = (1 + 4\pi^2 \ell^2 T^2)\cosh(2\pi n r_+/\ell) \pm 4\pi^2 \ell^2 T^2. \tag{3.24}$$

By performing the substitution $\Delta\tau = \frac{1}{2\pi T}(z - 2\pi n r_-/\ell)$, we can rewrite the response rate as

$$\mathcal{F}_{\mathrm{RBTZ}} = \frac{1}{4\pi\sqrt{2}} \sum_{n=-\infty}^{\infty} \eta^n \int_{-\infty}^{\infty} \mathrm{d}z \left[\frac{e^{-\frac{i\Omega}{2\pi T}(z - \frac{2\pi n r_-}{\ell})}}{\sqrt{\alpha_n^- - \cosh(z)}} - \zeta\frac{e^{-\frac{i\Omega}{2\pi T}(z - \frac{2\pi n r_-}{\ell})}}{\sqrt{\alpha_n^+ - \cosh(z)}}\right].$$

Computing the integrals, we can rewrite the response rate as

$$\mathcal{F}_{\mathrm{RBTZ}} = \frac{1}{4}\left[1 - \tanh\left(\frac{\Omega}{2T}\right)\right] \sum_{n=-\infty}^{n=\infty} e^{\frac{i\Omega n r_-}{\ell T}}\left[P_{-\frac{1}{2}+\frac{i\Omega}{2\pi T}}\left(\alpha_n^-\right) - \zeta P_{-\frac{1}{2}+\frac{i\Omega}{2\pi T}}\left(\alpha_n^+\right)\right]. \tag{3.25}$$

Note that we recover the static BTZ response rate when we have a vanishing inner radius, $r_- = 0$. The larger $0 < r_- \le r_+$ is, the greater the angular momentum of the black hole (and of the co-rotating detector).

18

3.2 Applying Open Quantum Systems

To compute the thermal Fisher information of our detector, we will make use of an open quantum systems framework applied to UDW detectors [57, 31, 26, 58]. Open quantum system evolutions allow for the interaction of a quantum system of interest, the UDW detector in our case, with an external system which we can then trace out to obtain the state of our system of interest.

Here, we couple our UDW detector to the vacuum state of the field before tracing the field states out. Employing the appropriate assumptions, we find ourselves capable of isolating the evolution of our detector.

Let us first define the total Hamiltonian of the joint system. This can be expressed as the sum of the interaction Hamiltonian along with the free Hamiltonian of both the detector and the scalar field:

$$H = H_D + H_\phi + H_I, \tag{3.26}$$

where $H_D = \frac{1}{2}\Omega a_D^\dagger a_D = \frac{1}{2}\Omega(|0_D\rangle\langle 0_D| - |1_D\rangle\langle 1_D|)$ is the free Hamiltonian of the detector with energy gap Ω, $H_\phi = \frac{dt}{d\tau}\sum_{\mathbf{k}}\omega_{\mathbf{k}}a_{\mathbf{k}}^\dagger a_{\mathbf{k}}$ is the free Hamiltonian of the scalar field evolving along the proper time of the detector, τ, and H_I is the interaction Hamiltonian described in Equation (2.3).

The time evolution (with respect to the proper time of the detector) is described by the von Neumann equation

$$\frac{\partial \rho_{\text{tot}}}{\partial \tau} = -i[H, \rho_{\text{tot}}], \tag{3.27}$$

where ρ_{tot} is the density matrix of the joint system. This joint system is initialized in the state $\rho_{tot}(0) = \rho_D(0) \otimes |0_\phi\rangle\langle 0_\phi|$, where $\rho_D(0)$ is the initial state of the detector and $|0_\phi\rangle$ is the conformal vacuum of the massless scalar field $\phi(x)$. To obtain the state of the detector, one must take the partial trace over the field of the joint density matrix, $\rho_D = \text{Tr}_\phi \rho_{tot}$.

Assuming weak coupling ($\lambda \ll 1$) with field correlations decaying sufficiently fast for large time separations, then the time evolution of the detector's density matrix can be expressed by the master equation of Kossakowski-Lindblad form [57]. This describes the most general Markovian time evolution of a quantum system [59], and is given by

$$\frac{\partial \rho_D(\tau)}{\partial \tau} = -i[H_{\text{eff}}, \rho_D(\tau)] + L[\rho_D(\tau)], \tag{3.28}$$

where $H_{\text{eff}} = \frac{1}{2}\tilde{\Omega}(|0_D\rangle\langle 0_D| - |1_D\rangle\langle 1_D|)$ is the effective Hamiltonian, and

$$L[\rho] = \frac{1}{2}\sum_{i,j=1}^{3} C_{ij}\left(2\sigma_j\rho\sigma_i - \sigma_i\sigma_j\rho - \rho\sigma_i\sigma_j\right), \tag{3.29}$$

is a dissipation term in which the σ_i are the Pauli matrices. The quantity $\tilde{\Omega}$ is a renormalized gap given by

$$\tilde{\Omega} = \Omega + i\left[\mathcal{K}(-\Omega) - \mathcal{K}(\Omega)\right], \tag{3.30}$$

where $\mathcal{K}(\Omega)$ is the Hilbert transform of the response per unit time $\mathcal{F}(\omega)$ defined by

$$\mathcal{K}(\Omega) = \frac{1}{i\pi}\,\text{PV}\int_{-\infty}^{\infty} d\omega\,\frac{\mathcal{F}(\omega)}{\omega - \Omega}, \tag{3.31}$$

with PV denoting the Cauchy principal value. C_{ij} is called the Kossakowski matrix, and is also completely determined by the response rate $\mathcal{F}(\Omega)$:

$$C_{ij} = \begin{pmatrix} A & -iB & 0 \\ iB & A & 0 \\ 0 & 0 & A+C \end{pmatrix}, \tag{3.32}$$

where

$$A = \frac{1}{2}[\mathcal{F}(\Omega) + \mathcal{F}(-\Omega)] \tag{3.33}$$

$$B = \frac{1}{2}[\mathcal{F}(\Omega) - \mathcal{F}(-\Omega)] \tag{3.34}$$

$$C = \mathcal{F}(0) - A \tag{3.35}$$

With this set up, the KL equation can be solved analytically. If we initialize our detector in the general pure state $|\psi_D\rangle = \cos\frac{\theta}{2}|0_D\rangle + \sin\frac{\theta}{2}|1_D\rangle$, its density matrix at time τ is specified by the Bloch vector $\boldsymbol{a} = (a_1, a_2, a_3)$ such that

$$\rho(\tau) = \frac{1}{2}\left(I + \boldsymbol{a}(\tau)\cdot\boldsymbol{\sigma}\right), \tag{3.36}$$

where $\boldsymbol{\sigma} = (\sigma_1, \sigma_2, \sigma_3)$ are the Pauli matrices, and the Bloch vector components are given by

$$a_1(\tau) = e^{-A\tau/2}\sin\theta\cos\tilde{\Omega}\tau, \tag{3.37}$$

$$a_2(\tau) = e^{-A\tau/2}\sin\theta\sin\tilde{\Omega}\tau, \tag{3.38}$$

20

$$a_3(\tau) = -e^{-A\tau}\cos\theta - R(1 - e^{-A\tau}). \tag{3.39}$$

where $R = B/A$ is a ratio of Kossakowski matrix elements. We note that A is the even part of the response rate with respect to the energy gap, Ω, while B isolates the odd part of the response rate. Interstingly, we will note that their ratio, $R = -\tanh(\frac{\Omega}{2T})$, is the same across all spacetimes considered in this thesis as well as for the (3+1)-dimensional spacetimes considered in [31]. This form can be intuited from a more detailed expression of R.

We note that in general the Bloch vector need not be a unit vector. In the case where $|\boldsymbol{a}| < 1$ we are left with a non-unitary evolution.

Now that we have identified our state of interest and its time evolution dynamics, we are in a position to compute the Fisher information for estimating the KMS temperature in AdS-Rindler along with the static and rotating BTZ black hole by using a UDW detector. The estimation strategy that we will employ consists of first letting the detector interact with the massless scalar field vacuum state in the appropriate spacetime background before making a projective measurement of the detector's state after some time τ in the detector's reference frame.

Since the UDW detector with which we are working is a two-level quantum state, it follows that every measurement of the state must have two possible outcomes. While our definition of the Fisher information in Equation (2.1) was expressed in terms of a continuous probability distribution, the definition is equally valid for a discrete probability distribution in which the integral becomes a sum.

Given that our system lives in a two-dimensional Hilbert space, this sum will have two terms with probabilities p and $1 - p$. The Fisher information can thus be expressed as

$$\mathcal{I}(\xi) = \frac{1}{p}\left(\frac{\partial p}{\partial \xi}\right)^2 + \frac{1}{1-p}\left(-\frac{\partial p}{\partial \xi}\right)^2 = \frac{1}{p(1-p)}\left(\frac{\partial p}{\partial \xi}\right)^2. \tag{3.40}$$

Measuring a state in the computational basis, $\{|0_D\rangle, |1_D\rangle\}$, results in the probability, p, of finding the detector in the state $|0_D\rangle$ to be a function of its Bloch vector. More explicitly, we have that

$$p = \text{Tr}(\rho |0_D\rangle \langle 0_D|) = \frac{1}{2}(1 + a_3), \tag{3.41}$$

while the probability of finding the detector in the state $|1_D\rangle$ is $1 - p = \frac{1}{2}(1 - a_3)$.

The Fisher information is thus given by

$$\mathcal{I}(\xi) = \frac{(\partial_\xi a_3)^2}{1 - a_3^2}, \tag{3.42}$$

where we can clearly see that it is only dependent on the third Bloch vector component, a_3, defined in Equation (3.39).

Since we are interested in examining the thermal Fisher information, we will set the underlying parameter ξ to be the KMS temperature T. We can thus express the thermal Fisher information as

$$\mathcal{I}(T) = \frac{(\partial_T a_3)^2}{1 - a_3^2}. \tag{3.43}$$

We will further rescale $\mathcal{I}(T)$ by T^2 in order to make it easier to compare values for varying T. We will denote this rescaled value simply by $\mathcal{I}$ (i.e., $\mathcal{I} = \mathcal{I}(T)T^2$) and we will henceforth refer to this simply as the Fisher information. Note that this rescaling also results in the Fisher information being unitless.

Before moving on to our results section, we will identify all of the parameters that will be featured in our analysis. Note that we will be expressing all parameters in terms of the AdS length, ℓ.

The first parameters worth noting are the detector energy gap, Ω, and the KMS temperature, T. These both have units of inverse length so we will multiply them by the AdS length to make them unitless. They will thus be labelled in plots as $\Omega\ell$ and $T\ell$. It is also worth noting that the energy gap only ever appears in the response rate as a ratio with the temperature Ω/T; thus their relative values will be of interest to us. We will refer to set ups as being 'hot' if $T > \Omega$ and 'cold' if $T < \Omega$.

We also note that while we have accelerations, a, and radial positions, R_D, in our derivations, these are always related to the temperature and the BTZ mass, M. As such, acceleration and radial position will not be featured prominently in our analysis, since we are more interested in understanding how our results pertain to the KMS temperature and the BTZ mass.

The remaining general parameters are the initial state of the detector, θ, which we will often fix to one of $\{0, \pi/2, \pi\}$, the detector interaction time, τ, which we will scale by the AdS length as τ/ℓ, and the spacetime boundary condition, parametrized by ζ, which can be one of $\{0, 1, -1\}$ corresponding to the transparent, Dirichlet, and Neumann boundary conditions respectively.

In the BTZ spacetimes, the dimensionless BTZ mass M will be a very important variable, while in the rotating BTZ spacetime we will also consider the angular momentum, J, which we will express in terms of $M\ell$. Note that one can equivalently describe BTZ black holes in terms of the inner and outer radii, r_- and r_+, but we find this perspective less informative and opt to describe the black hole in terms of its mass and angular momentum instead.

Chapter 4

Results

In this chapter, we will present the results of our Fisher information analysis of black hole spacetimes. To do this, we will first present our analysis of the thermal Fisher information in (2+1)-dimensional AdS spacetime. This will not only set the scene for our black hole analysis by providing us a background against which we will be able to highlight genuine black hole effects, but it will also allow us to compare our results to those obtained in (3+1)-dimensional spacetime [31]. In so doing, we will note that the Fisher information of AdS space was not quite as exciting as it was previously purported to be.

Having set the stage, we will then proceed to the real meat of this thesis: the first Fisher information analysis of a black hole spacetime. We will first consider the static (2+1)-dimensional black hole, allowing us to consider the role that the BTZ mass plays in the Fisher information, before considering the angular momentum contribution to the Fisher information for rotating BTZ black holes.

Our analysis of the Fisher information here will be largely qualitatively driven. This is in part owing to the fact that the analytic expressions for the response rate (and ultimately the Fisher information) are dependent on Legendre polynomials with complex indices for which we have limited intuition. Our analysis does however accomplish two goals.

First, given a specific spacetime and some known detector parameters (e.g., intial state, energy gap), we can identify the time at which we should perform the measurement to obtain the best estimate of the temperature. Second, we want to be able to use the Fisher information as a probe of the underlying spacetime. By this we mean to ask, given a particular Fisher information behaviour, can we discriminate between the possible background spacetimes? We find that we are indeed able to distinguish between spacetimes, with particular success when it comes to identifying the black hole mass.

4.1 Anti-de Sitter Spacetime

We will begin our analysis by considering the Fisher information of a constantly accelerating detector in AdS spacetime, or equivalently a stationary detector in AdS-Rindler. Since we are considering a supercritical acceleration, there will always be a thermal response and non-zero response rate.

As a first step, we will consider the possible qualitative behaviours that the temporal Fisher information, i.e., the (thermal) Fisher information as a function of time τ, might have. In Figure 4.1, we observe at first glance nine qualitatively distinct behaviours. While these alleged nine behaviours were previously identified by Du and Mann [31], there remain a few noteworthy observations.

Most importantly, we note that there are not in fact nine qualitatively distinct behaviours as was previously claimed, but only eight. If we number the plots in the grid 1 through 9 as on a telephone number pad, we can see that behaviours 3 and 4 are qualitatively identical. They both begin at zero, then smoothly increase into and decrease out of a global maximum, before asymptoting to some positive value. Since this asymptotic behaviour was not clear in our behaviour 4 plot, we included an inset image to show that the asymptotic behaviour is non-zero. We were also able to show this in (3+1)-dimensional AdS, resulting in a slight correction to previous results.

While one might suspect that the Fisher information is never zero after this observation, we were able to verify that the minima in behaviours 5 and 6 do indeed attain 0, at least to high numerical certainty, as shown by the inset in behaviour 6.

This does raise some interesting questions. It is clear that the Fisher information cannot take on negative values; this can be realised mathematically due to the prominent presence of terms being squared in the definition, or physically by noting that the Fisher information quantifies the knowledge we might be able to extract about the temperature from the measurement of the state of our detector. Clearly, one could not have negative information about this; the worst one could do is to have no information about the underlying parameter gleaned from the observable measurement.

It does seem peculiar however that at a certain time $\tau \neq 0$ the Fisher information is 0 when it is non-zero on either side of this time. What is it about that particular time that results in a total loss of information? It is interesting to note here that the only difference between the parameters for behaviours 3 and 6 is the initial state of the detector.

To further delve into the possible qualitative behaviours, we note that they always start at the origin. This is sensible because we do not expect our detector to have any

information about the temperature until it begins its evolution coupled to the vacuum state of the field. It is also unsurprising to see that the Fisher information plateaus to
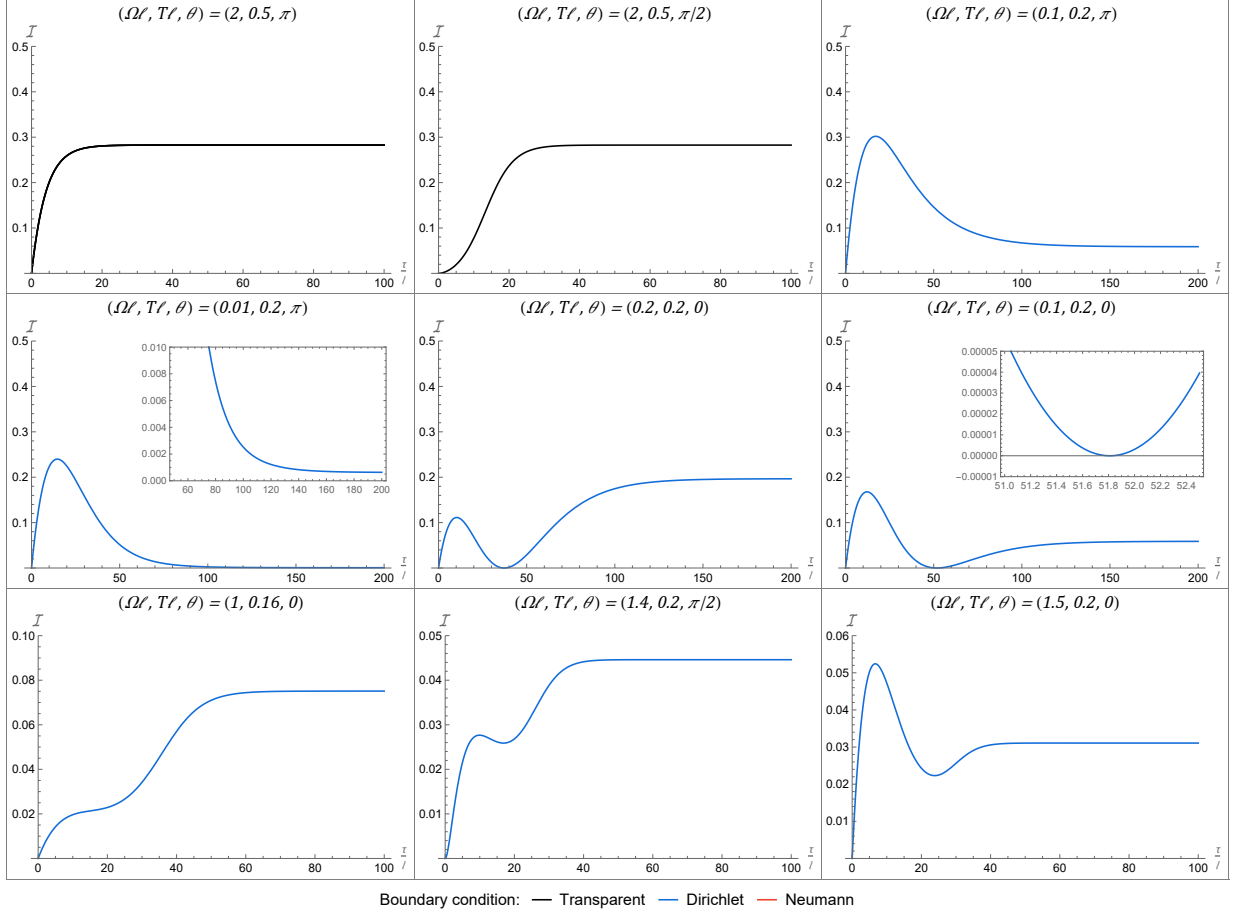

Figure 4.1: This grid plot of the temporal Fisher information displays all the distinct behaviours observed for our detector in AdS Rindler. From left-to-right and top-to-bottom, we label these as behaviours 1 through 9. There are eight distinct behaviours, with behaviours 3 and 4 being the same qualitatively. We note that while both the Dirichlet and Neumann boundary conditions ($\zeta = 1$ and $\zeta = -1$ respectively) can be used to obtain all nine behaviours, only the first two can be obtained from the more fundamental transparent boundary condition ($\zeta = 0$). To highlight this fact, we have plotted the first two behaviours using the transparent boundary condition (in black), while the remaining six qualitatively distinct behaviours were plotted using the Dirichlet boundary condition (in blue).

25

some positive value at sufficiently large times. This can be understood as corresponding to the thermalization of the detector after which there is no further information to be gleaned from the field.

What is more interesting, and thus harder to explain, is the behaviour between these start and end points. While the Fisher information obviously needs to increase to reach its plateau from the origin, it is not required to do so monotonically. There appears to at most two inflection points between the origin and the plateau. This allows for either a single (global) maximum from which the Fisher information decreases with time to reach its asymptotic value, or it can have both a maximum and minimum before reaching its asymptotic value. This latter case corresponds to four of the possible behaviours (the maximum can either be above or below the asymptotic value and the minimum can either zero or non-zero).

The last thing to note about the plots in Figure 4.1 is the colour of the Fisher information curves. The first two behaviours are depicted with a black curve corresponding to the transparent boundary condition ($\zeta = 0$). We consider this to be the 'most basic' boundary condition in a sense because it completely eliminates a term from our response rate in Equation (3.8). As such, we expect it to convey the most fundamental behaviours of our system. In (2+1)-dimensional AdS, it is only these two most basic behaviours that are achievable using the transparent boundary condition. The remaining six behaviours cannot be obtained with the transparent boundary condition, though they can be achieved with either Dirichlet ($\zeta = 1$) or Neumann ($\zeta = -1$) boundary conditions. (We have chosen to use the Dirichlet boundary conditions here for no particular reason.)

While the number of distinct qualitative behaviours remains the same between (3+1)- and (2+1)-dimensional AdS, behaviours 1 through 6 can all be achieved using the transparent boundary condition in 3+1 dimensions. In this sense, there is some loss of generality when we reduce the number of spacetime dimensions in which our detector is operating.

Having identified the set of possible behaviours, let us now hone in on what characterizes these behaviours. We have already noted that the sole difference between behaviours 3 and 6 in Figure 4.1 is the state in which the detector was initialized. In Figure 4.2, we display the Fisher information for a subset of the parameter space of our system, such that each plot specifies a particular set of initial conditions. We attempt to lay these plots out in such a way as to convey the most relational information. This is primarily encoded across rows and across columns.

The first thing to note is that the value of the asymptotic Fisher information is not dependent on the choice of boundary condition, since the asymptotic value in any given plot is the same. Furthermore, we can note that the asymptotic value is not dependent on
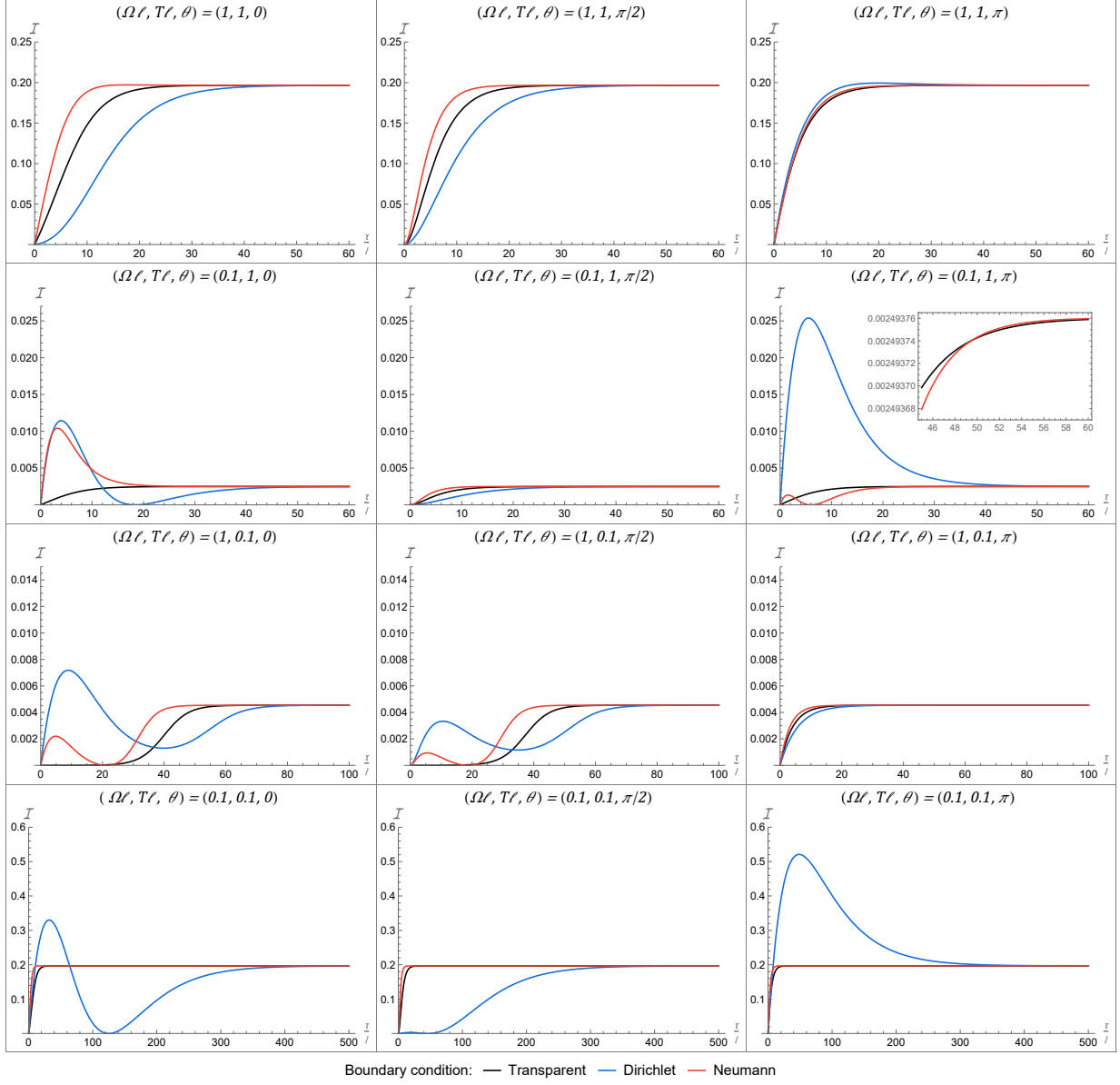
Figure 4.2: This grid plot displays the temporal Fisher information in AdS for all boundary conditions for various parameter choices. Each row of this grid plot fixes a pair of energy gap and temperature parameters, $(\Omega\ell, T\ell)$, while each column fixes an initial state of the detector, θ. Across all plots the colour of the curves represent the boundary condition.

the initial state of the detector (which varies across columns) since the asymptotic value is fixed for every row. We thus expect the asymptotic value to be dependent only on the temperature, T, and the energy gap of the detector, Ω.

In fact, it is straightforward to show that the asymptotic Fisher information only depends on the Kossakowski ratio, R, and the KMS temperature, T. To see this, we note that $\lim_{\tau \to \infty} a_3 = -R$. We can then show that

$$\lim_{\tau \to \infty} \mathcal{I} = \lim_{\tau \to \infty} \frac{(\partial_T a_3)^2}{1 - a_3^2} T^2 = \frac{(\partial_T R)^2}{1 - R^2} T^2, \tag{4.1}$$

where the Kossakowski ratio is $R = -\tanh(\Omega/2T)$.

Computing this explicitly, we find that the asymptotic Fisher information is given by

$$\mathcal{I}_{\text{asym}} = \frac{\Omega^2}{2T^2} \operatorname{sech}^2\left(\frac{\Omega}{2T}\right), \tag{4.2}$$

which is dependent only on the ratio Ω/T. This dependence on the ratio of the energy gap to the temperature, rather than on their independent values can be seen by comparing the first and last rows of Figure 4.2, where the ratios are the same despite the parameter values being distinct.

From this, one can see that there is an optimal ratio Ω/T that results in the largest asymptotic Fisher information. This ratio is given by $\Omega/T = 2x_0$, where $x_0 \approx 1.2$ is the solution to $x_0 \tanh x_0 = 1$.

The final observation that we are capable of making from Figure 4.2 is that while all three boundary conditions approach the same asymptotic value, the Neumann and Dirichlet boundary conditions appear to sandwich the transparent boundary condition from above and from below respectively. This agrees with the intuition provided by Avis, Isham, and Storey whereby the transparent boundary condition is a superposition of sorts of the Neumann and Dirichlet boundary conditions [60].

4.2   Static BTZ Spacetime

As we progress to analysing the Fisher information of a stationary UDW detector outside a static BTZ black hole, we recall that the $n = 0$ term from the response rate's image sum in Equation (3.17) corresponds to the AdS response rate for a BTZ mass of $M = 1$. We will thus begin this section by restricting ourselves to the case in which the mass is

unity in order to identify what Fisher information behaviours can truly be attributed to the presence of the black hole. From there, we will proceed to examine what effects varying the mass has on the Fisher information, which we find to be rather interesting.

4.2.1   Fisher information analysis for $M = 1$
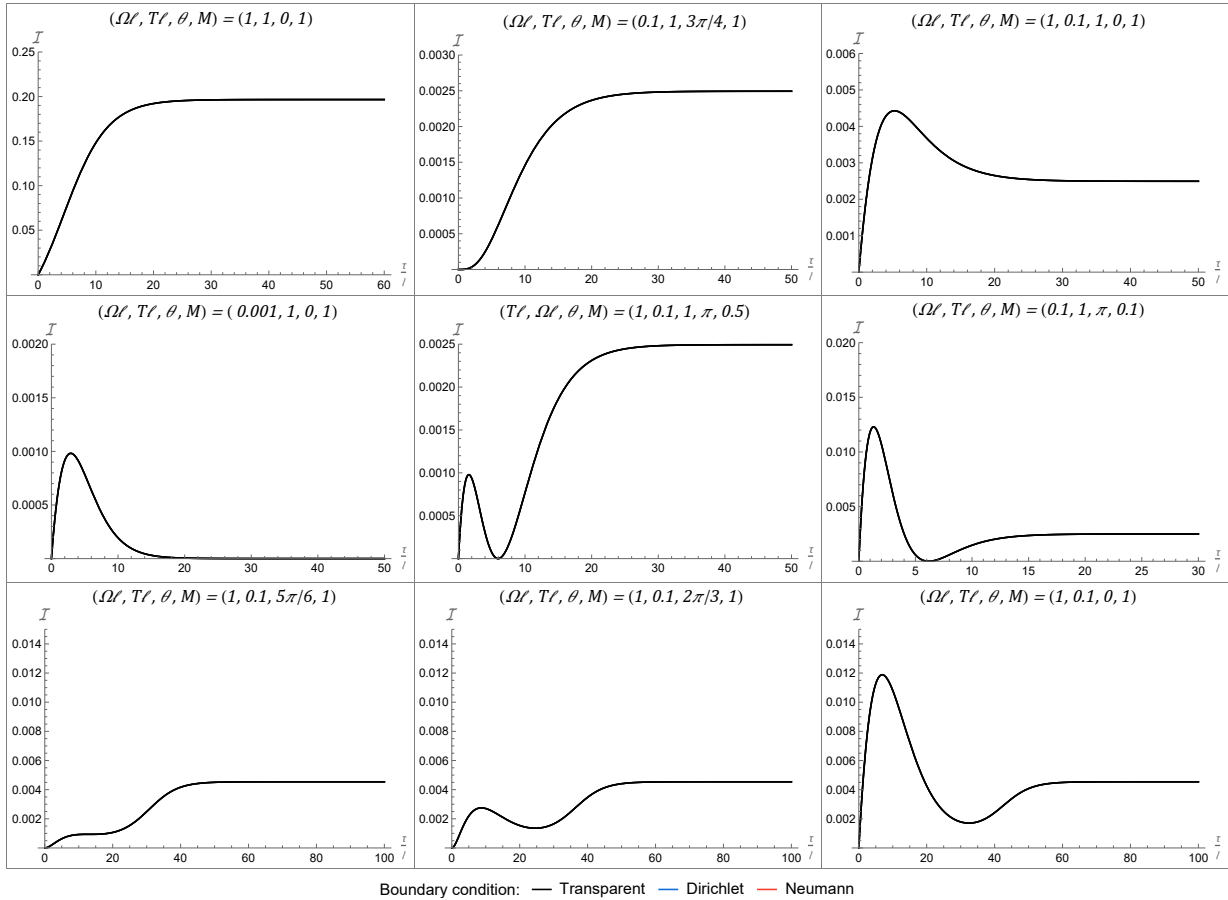
Figure 4.3: All previously identified qualitative behaviours can be reproduced in the BTZ spacetime. All of the behaviours displayed here were obtained using only the transparent boundary condition (in black). Each can also be achieved using either Dirichlet or Neumann boundary conditions.

We summarize the possible qualitative behaviours that the Fisher information can take on from our stationary detector in BTZ spacetime in Figure 4.3. Unsurprisingly,

we are able to recover all of the distinct qualitative behaviours identified in Figure 4.1, though we are able to obtain all of them using the transparent boundary condition, in addition to the Dirichlet and Neumann boundary conditions. This is the first way in which we find that we are able to distinguish between spacetimes based solely on the Fisher information from our detector. Stated more explicitly, it is clear that if we observe any of the qualitative behaviours 3 through 9 in a (2+1)-dimensional spacetime with transparent boundary conditions, we can state with certainty that we are not in AdS and thus intuit that we are in the presence of a black hole.

While we did choose mass values that were different than one for our displays of behaviours 5 and 6, these behaviours were present for a unit mass, though they were less clear than for our choice of parameters. Besides allowing for the discrimination between spacetimes, the presence of more complicated Fisher information behaviours in the BTZ spacetime for even the transparent boundary condition is indicative of the added complexity of the BTZ spacetime, even for unit mass.

Having the range of possible behaviours being maximal in the sense that it is as large as possible (there are no more possible behaviours, and all behaviours can be observed for all boundary conditions), let us compare the behaviours in the BTZ spacetime directly from those observed in AdS for specific choices of parameters. In particular, it is possible that while the span of possible behaviours is similar overall, that their manifestations given a certain set of parameters is dramatically distinct.

In order to perform this analysis, we turn to Figure 4.4 where we display the Fisher information for the BTZ spacetime across the same subset of phase space as we had previously considered for AdS. We plot solid lines representing the BTZ Fisher information atop of the dotted lines representing the AdS Fisher information to allow us to observe any changes between the two. Throughout this plot we restrict the BTZ mass to $M = 1$ in order to isolate the most basic black hole perturbations.

It becomes apparent that when the energy gap is equal to the temperature there is almost no difference between the Fisher information for the AdS and BTZ spacetimes. Since this behaviour is present across the entirety of the first and fourth row, it is clear that the initial state of the detector is not at play. If these were perfectly equal, then it would mean that the $P_{-\frac{1}{2}+\frac{i\Omega}{2\pi T}}(\alpha_n^{\pm})$ terms are either zero or they must cancel themselves.

If these terms were to cancel out, it would have to be with respect to the n parameter since the behaviour holds for all ζ. It is straightforward to see that $\alpha_{-i}^{\pm} = \alpha_i^{\pm}$ by virtue of the hyperbolic cosine being an even function. We thus conclude that it is likely that the Legendre polynomial and ensuing terms converge quite quickly to zero. This can indeed be verified numerically.
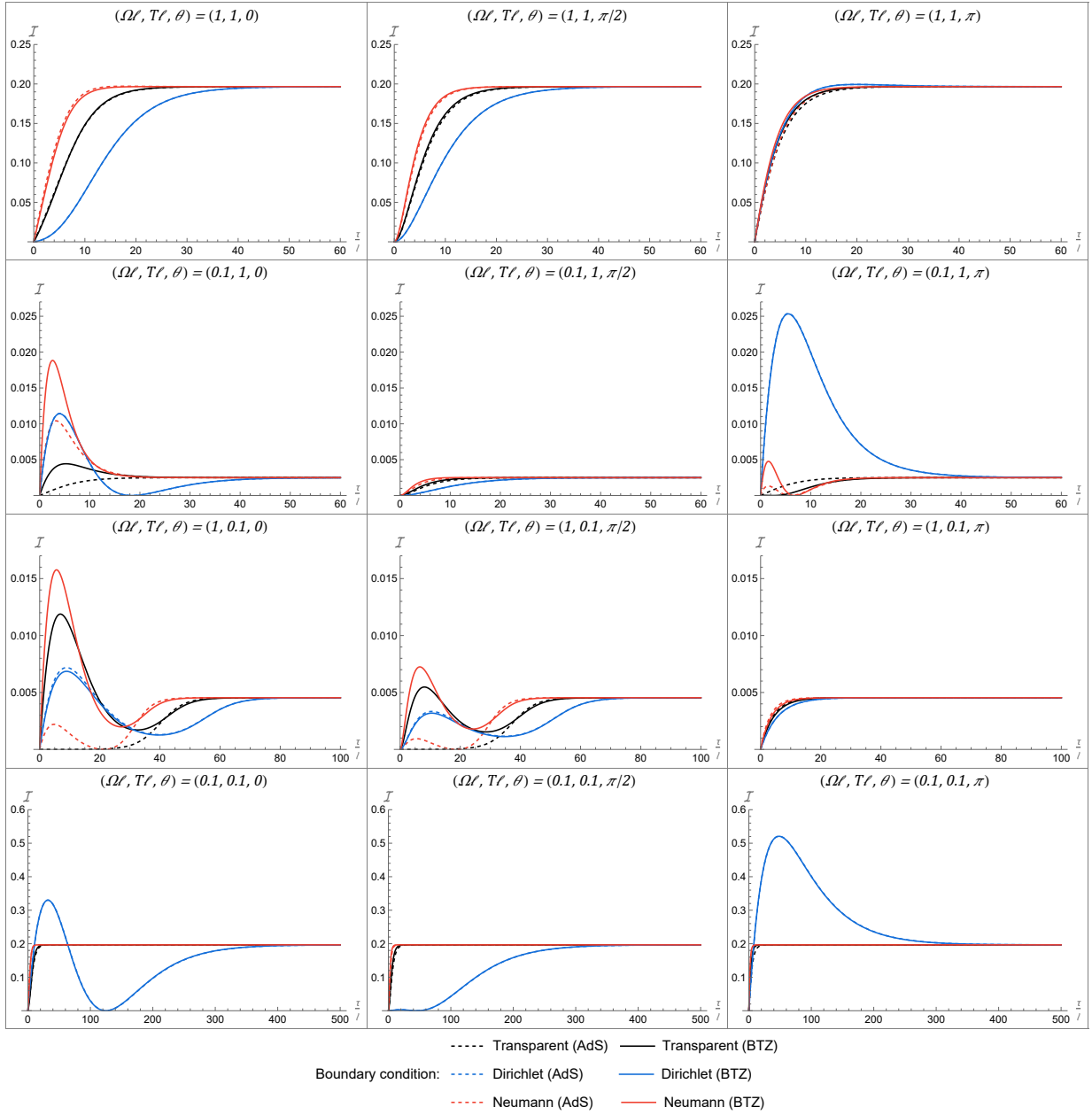
Figure 4.4: Here we directly compare the Fisher information in BTZ (solid lines) with the Fisher information in AdS (dashed lines) that was previously presented in Figure 4.2. The layout and choice of parameters is the same: the initial state of the detector, θ, varies across columns, while the temperature, $T\ell$, and energy gap, $\Omega\ell$, vary from row to row. The mass parameter for the BTZ spacetime is set to $M = 1$ throughout this grid.

31

We also note that for $n \geq 1$, we have that $\alpha_n^+ \approx \alpha_n^-$ since the cosh term dominates each expression. This means that for Dirichlet boundary condition ($\zeta = 1$), there is minimal change between the AdS and BTZ spacetimes, since the Legendre polynomial terms cancel each other.

As such, while the transparent boundary condition allows for definitive spacetime discrimination based on the qualitative behaviour of the Fisher information, provided the proper energy gap to temperature ratio, this is distinctly impossible for the Dirichlet boundary condition (provided a BTZ mass of unity).

Lastly, we draw attention to the Neumann boundary condition ($\zeta = -1$). In general, the Fisher information associated to the Neumann boundary condition sees a sizable increase. It is curious to note that in the 'cold' set up, the initial peak in the Fisher information occurring at early times appears to be suppressed by the initial state of the detector, with no visible peak for any boundary condition, in any spacetime, for $\theta = \pi$.

4.2.2 Fisher information analysis for varied M

Having characterized the Fisher information behaviour across phase space and having compared it with the analogous behaviours from AdS, we now delve into an analysis of the parameter that is not present in AdS: the mass. In order to do this, we have limited ourselves to masses varying between $M = 0.01$ and $M = 1.5$. Conceptually, we find that this range encompasses the behaviours of the mass well enough, with rapid convergence of behaviours for large masses ($M > 1$), while we notice a fair bit of exciting behaviour for the small masses ($M < 1$). Pragmatically, computing the response rate (and thus the Fisher information) for small masses requires a large number of terms in the image sum to be confident about the convergence. This results in longer run times for the computer. On the other end, for large masses, we must use fewer terms in our sum or else our approximation in Mathematica returns an "Indeterminate" value owing to the large term in the Legendre polynomial (this goes to zero) So we can preserve convergence, but it means that we cannot use a single function across any mass and have consistently accurate results.

To do this we have plotted the Fisher information for masses varying between $M = 0.01$ and $M = 1.5$, noting that for large masses (above $M = 1$) there is little to no change in in the Fisher information.

We begin our analysis of the Fisher information for varying mass by considering a subset of phase space for which $\Omega = T$. In particular, for Figure 4.5 we set both the energy gap and the temperature to be 0.1, though the trends observed generalize to other values so long as their ratio remains unity.
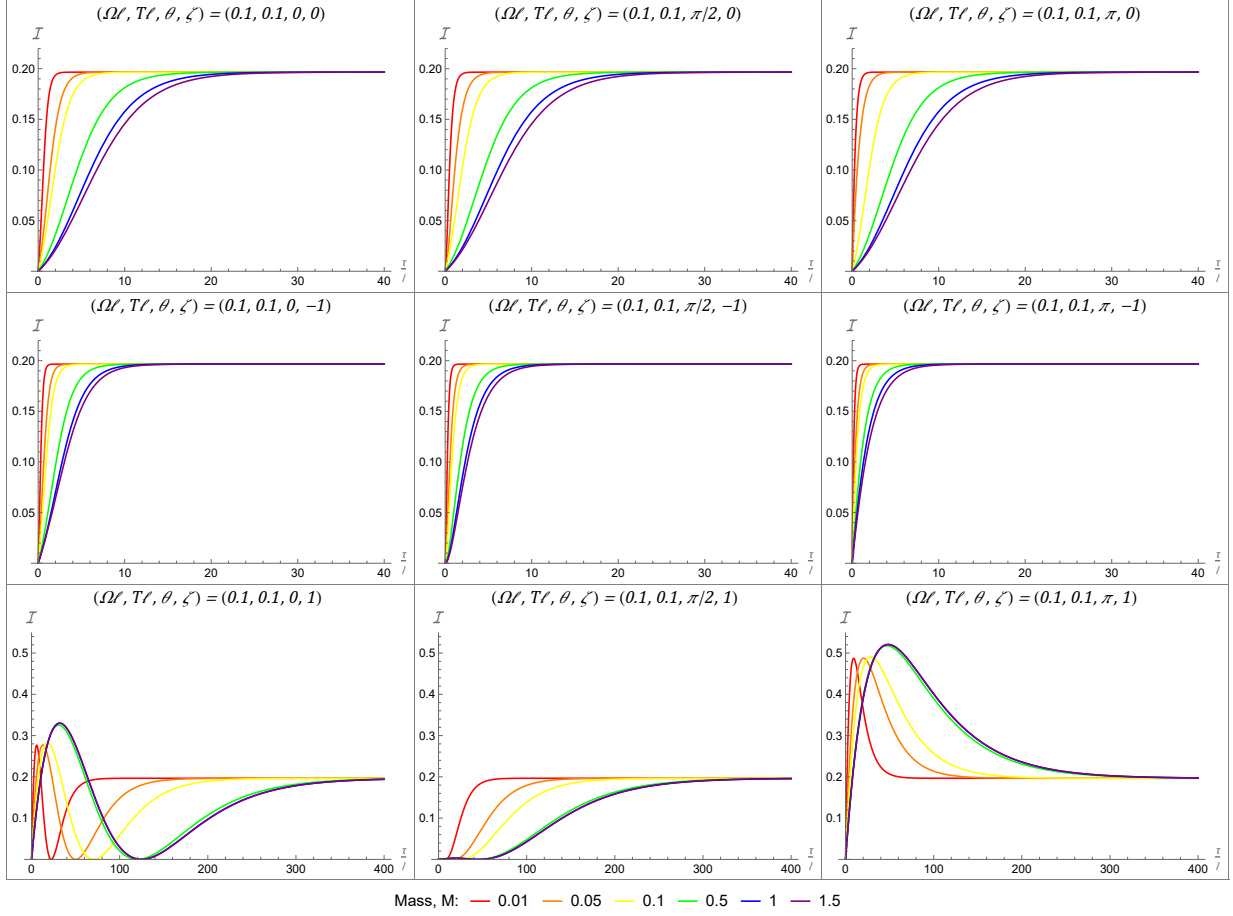
Figure 4.5: This grid of plots depicts the effect of the BTZ mass, M, on the Fisher information. Increasing mass corresponds to progressing along the colours of the rainbow (ROYGBV), ranging from $M = 0.01$ to $M = 1.5$. The energy gap, temperature, are fixed and equal throughout the grid. Each column represents a different initial state of the detector, while each row represents a different boundary condition for the spacetime. We note that for $\Omega\ell = T\ell = 0.1$ a variation of the mass parameter does not seem to have a substantial effect on the Fisher information. Increasing mass seems to delay the increase in Fisher information, with a slight increase in the maximum value for the Dirichlet boundary condition.

To make our comments on the grid plot in Figure 4.5 more digestible, we note that the columns still correspond to the initial state of the detector $\theta = \{0, \pi/2, \pi\}$, but we have now fixed the values of Ω and T throughout the entirety of the grid plot and we have instead varied the boundary condition from row to row. The first row corresponds to the transparent ($\zeta = 0$) boundary condition, followed by the Neumann ($\zeta = -1$) boundary condition and finally the Dirichlet ($\zeta = 1$) boundary condition. The colour of the curves represent the value of the mass parameter, with M increasing from 0.01 to 1.5 along the colours of the rainbow (ROYGBV).

Following the colours of the rainbow, it is easy for us to see that there is a smooth, monotonic shift in the Fisher information as we increase the mass parameter by two orders of magnitude. This shift delays the arrival of the maximal Fisher information across the board and even results in a slight increase of it for the Dirichlet boundary condition. There is no change in the Fisher information's qualitative behaviour when varying M for $\Omega\ell = T\ell = 0.1$.

We note that these trends were consistent when we considered other values of $\Omega = T$. We thus conclude that once again there are special patterns in the Fisher information behaviour when $\Omega = T$. Determining how special these trends are requires us to examines what happens when $\Omega \neq T$.

When we move away from the equilibrium ratio between the energy gap and the temperature, we notice that we lose any semblance of monotonicity as seen in Figure 4.6. While one may look at the Fisher information for this 'cold' set up and initially think that there is some degree of smoothness, this notion is quickly dispelled upon closer examination.

If we track the change in mass in any one of the plots in Figure 4.6 by following the colours of the rainbow, we note that between $M = 0.01$ and $M = 0.1$ there appears to be some degree of monotonicity. However, this trend is abruptly halted by the increase in the Fisher information between $M = 0.1$ and $M = 0.5$, in contrast with the previous decreasing trend. Beyond this reversal, the direction in which the Fisher information is evolving is changes twice more before reaching a final value for $M = 1.5$.

Across a given row (i.e., for a fixed ζ) in Figure 4.6, we notice the previously observed trend in the cold set up (from Figure 4.4) of the Fisher information's local maximum decreasing as the initial state of the detector goes from $\theta = 0$ to $\theta = \pi$. This trend persists across all mass values and appear to occur at a proportional rate, i.e., the maximal Fisher information is reduced by a fixed proportion based solely on the initial state of the detector independent of the mass.

Upon closer examination of the mass-induced Fisher information variations in the cold set up, we find that the increases and decreases in the Fisher information's value resemble
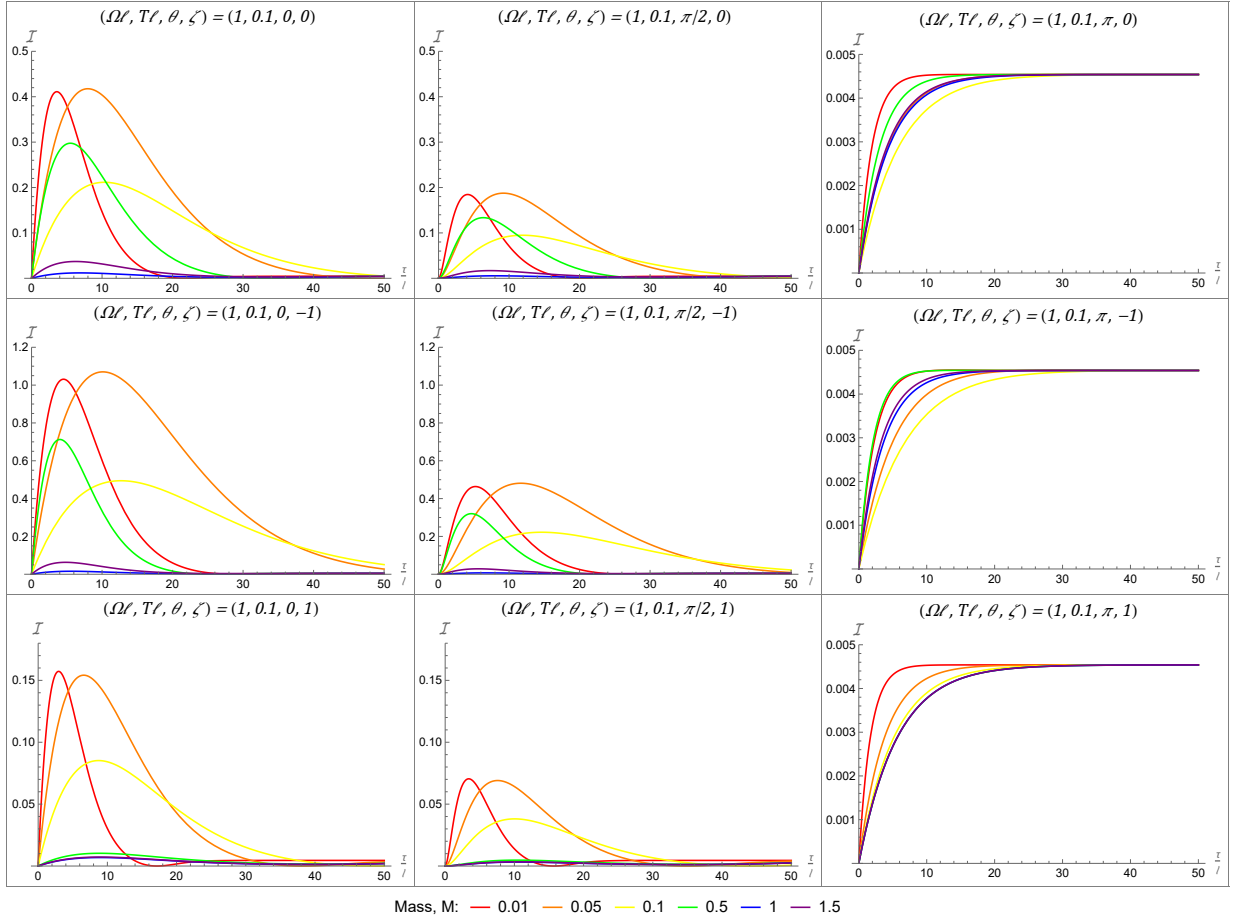
Figure 4.6: We consider the effect of a variation in mass parameter, M, on the Fisher information given our 'cold' set-up where $\Omega\ell = 1$ and $T\ell = 0.1$. This grid is set-up much like that displayed in Figure 4.5, except that $\Omega \neq T$. This leads to non-monotonic behaviour when varying M. In particular, for $\theta = 0$ and $\zeta = 0$ we see a smooth evolution from the red curve to the yellow one, but there is a change of direction as the Fisher information jumps back up from yellow to green. It then continues along its path down to the blue curve before jumping up once more to the purple curve. When considering the effect of the mass parameter more closely, we see that the Fisher information does indeed experience these two jumps. In fact, while these seem to be the only jumps, they are even more extreme than what is made visible here. Note that the $\mathcal{I}$-axis in the rightmost column (corresponding to $\theta = \pi$) has been rescaled by one to three orders of magnitude relative to the other two columns to highlight the behaviour of the Fisher information before it asymptotes.
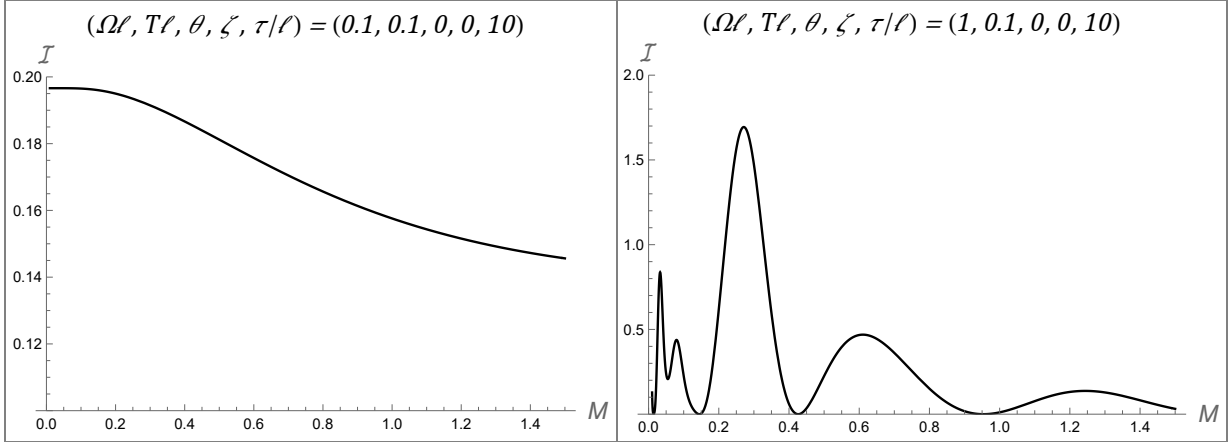
35

a damped oscillation of sorts.

Figure 4.7: Delving into the mass dependence of the Fisher information for varied energy gap to temperature ratios, we contrast the first plots from Figures 4.5 and 4.6. For a fixed time, $\tau/\ell = 10$, we can see that when $\Omega = T$ the Fisher information is monotonically decreasing with increasing mass, while it oscillates rather dramatically when $\Omega\ell = 1$ and $T\ell = 0.1$.

We have fixed the time parameter in Figure 4.7 in order to hone in on a more smooth depiction of the mass variation on the Fisher information. We see that is indeed smooth and monotonically decreasing in the case of $\Omega = T$, whereas is oscillatory for $\Omega \neq T$. In fact, these peaks and troughs go much beyond what was initially depicted in Figure 4.6. So much so that they allow for a rather successful identification of the BTZ mass, provided we know the other variables. In particular, if the Fisher information is zero, then it must be in one of the troughs corresponding to particular masses. Similarly, if we have a large Fisher information we can narrow down the mass of our black hole to one of the peaks. The larger the Fisher information, the fewer eligible peaks and the more restrictive within these we can be.

We have made it clear in the previous three figures that the ratio between the energy gap and the temperature is a key factor in determining the effect that the BTZ mass has on the Fisher information; much more so than either initial state of the detector or the boundary condition of the spacetime. But we might still wonder how does this ratio affect the mass variation in general? Is it not possible that we simply chose two particular values that displayed very distinct behaviours?

To answer this question, we will turn to a series of density plots for which we fix the
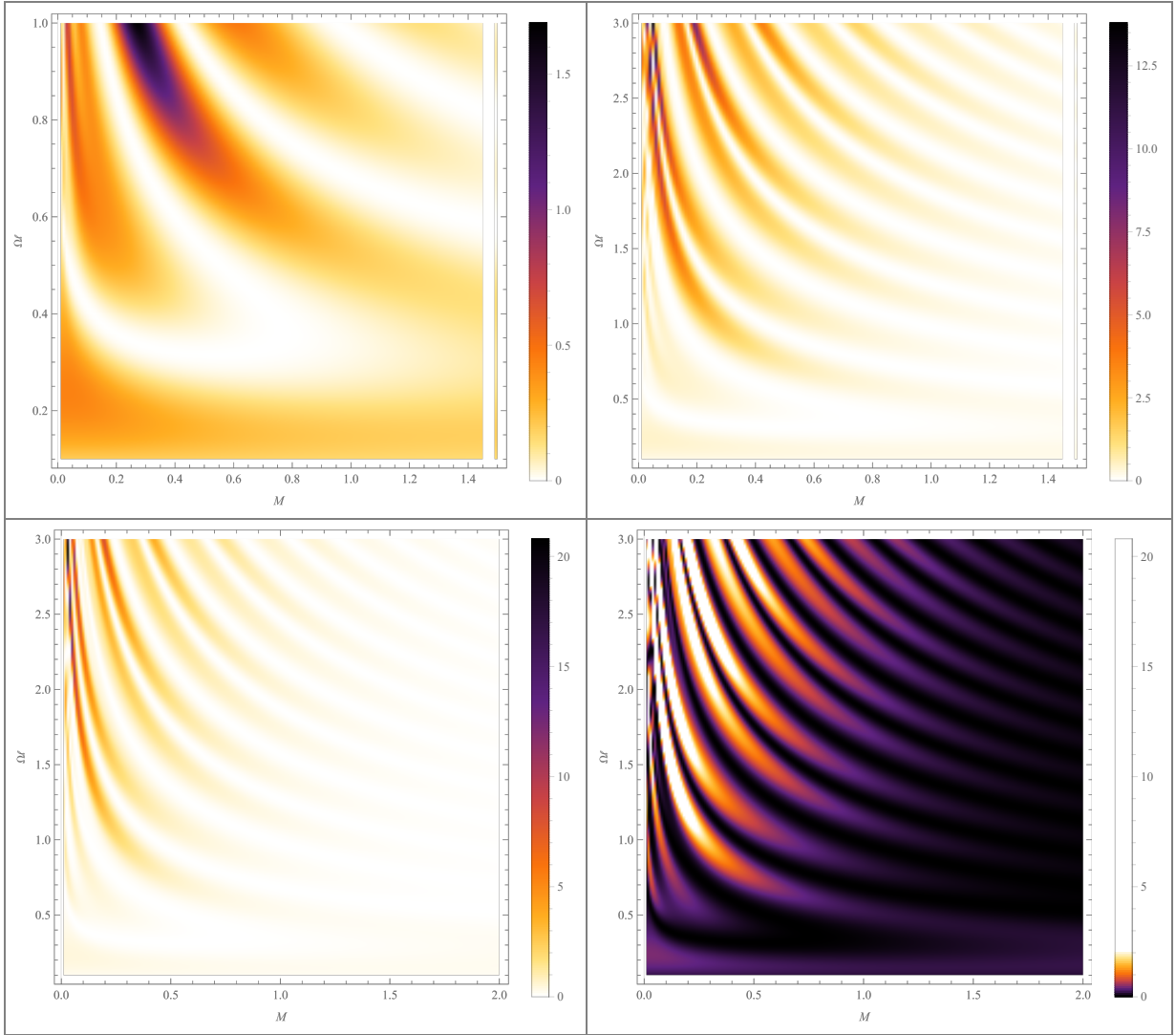
Figure 4.8: We plot the Fisher information with respect to the energy gap, $\Omega\ell$, and the mass, M. Held constant across these plots are $T\ell = 0.1$, $\theta = 0$, $\zeta = 0$, and $\tau/\ell = 10$. Note that these are the same values as in Figure 4.7 and that these density plots can actually be seen as an extension of this previous figure. In the top-left plot, we have simply extrapolated the Fisher information for varying $\Omega\ell$ between the curves depicted in Figure 4.7. In the top-right plot, we have extend these result for larger energy gaps, up until $\Omega\ell = 3$. The bottom two plots depict the same data, but have different colour gradients that draw our attention to different parts of the plots. In the bottom row, we have extended the results up until $M = 2$.

time and temperature while varying the energy gap and mass. In the top-left plot of Figure 4.8, we extrapolate between the two curves depicted in Figure 4.7, plotting the Fisher information for $0.01 \leq M \leq 1.5$ and $0.1 \leq \Omega\ell \leq 1$. We notice an interesting 'wave' pattern that does extend beyond the case where $\Omega\ell = 1$, $T\ell = 0.1$. In the top-right plot of Figure 4.8, we have simply increased the range of values $\Omega\ell$ can take up to 3. Doing so, we see that the 'wave' pattern extends into phase space, with the maximal Fisher information increasing along with the energy gap. We also note that for a fixed Ω, the number of oscillations in the Fisher information from $M = 0.01$ to $M = 1.5$ increases.

The two plots in the bottom half of Figure 4.8 both represent the same data, but we have reduced the number of image sum terms in our numerical representation of Equation (3.17) from 11 terms (corresponding to $n = \pm5$) to 7 terms (corresponding to $n = \pm3$) in order to examine masses up to $M = 2$. Doing so does however reduce the convergence of the Fisher information for small masses (hence the increase in the maximal Fisher information from the top-right to the bottom-left plots of Figure 4.8). The qualitative behaviour appears to have remained unchanged though. To better see the wave pattern in the bottom row, we have modified the colour scale to focus on where the Fisher information is relatively small. In so doing, we note that the wave pattern does indeed extend into the phase space for larger masses, though its effects are dampened.

These density plots seem to suggest that the case where $\Omega = T$ is indeed special in the sense that it does not have any oscillations. In contrast, the 'colder' our set up (i.e., the larger Ω is relative to T), the more extreme the oscillations in both frequency and magnitude.

The wave pattern seen in Figure 4.8 can be exploited to help identify the BTZ mass of an otherwise known set-up by looking at where the peaks and troughs occur. It also shows the importance of tuning the detector's energy gap relative to the temperature in order to maximise the Fisher information and how this is very much mass-dependent.

4.3   Rotating BTZ Spacetime

Having shown in the previous section the effect of the black hole mass on the Fisher information, and how the Fisher information can tell us about what mass might be present, we will now turn our attention to another key parameter of a black hole spacetime: its angular momentum.

It is known that the angular momentum of a black hole can have significant impact on the properties of the quantum vacuum as perceived by a coupled UDW detector. In

particular, the entanglement(concurrence) between two detectors can be dramatically increased, with a more pronounced effect for near-extremal rotating black holes [16], while rotation also amplifies or dampens the anti-Hawking effect for small mass black holes [61].

Here we find that the Fisher information increases most between $J = 0.5M\ell$ and $J = 0.95M\ell$. This is in line with results for the transition probability, while the concurrence increases most for $J \geq 0.99M\ell$ [16].

In our analysis of the rotating BTZ black hole, we were able to recover all of the qualitative behaviours described in Figure 4.3, and we were unable to identify any new behaviours. Since we can always recover the results from the stationary detector near a static black hole by setting the angular momentum, J, (or equivalently, the inner radius, r_-) equal to zero, we will not bother duplicating Figure 4.3. The fact that we were unable to identify any new qualitative behaviours suggests that there are at most one local maximum and minimum per behaviour, though there is no clear physical intuition into this constraint.

In order to perform a sufficiently thorough analysis of the angular momentum's effect on the Fisher information as succinctly as possible, we will limit ourselves to the cases where the BTZ mass is either unity or small at $M = 0.01$.

Beginning with the more simple case for which $M = 1$, we found that there was significant variance in the effect of rotation on the Fisher information depending on the ratio between the energy gap of the detector and the temperature, as well as depending on the boundary condition at infinity. While there was some variance with respect to the initial state of the detector, this was expected based on previous variations with respect to θ, so this will not be a focus of our analysis in this section. In particular, we will assume that our detector is initialized in the ground state for the rest of this section.

We summarize the effects of rotational variance on the Fisher information for $M = 1$ in Figure 4.9. Since we are no longer varying the initial state of the detector, we have chosen to vary the ratio Ω/T within a given grid plot in addition to varying the boundary condition. Here, we have encoded the Ω/T ratio within the rows, since the ratio defines a fixed asymptotic value for the Fisher information, while we have encoded the boundary conditions, $\zeta = \{0, -1, 1\}$, across the columns. The mass, $M = 1$, and initial state, $\theta = 0$, are both fixed throughout the grid.

Moving across either rows or columns, we can identify some interesting patterns. If we first restrict ourselves to the change in behaviour from column to column, corresponding to different boundary conditions, we can see the previously noted point that the transparent and Neumann boundary conditions, corresponding to the first and second column respectively, are quite similar in many respects, whereas the Dirichlet boundary condition in the third column displays entirely different qualitative behaviours. The most glaring
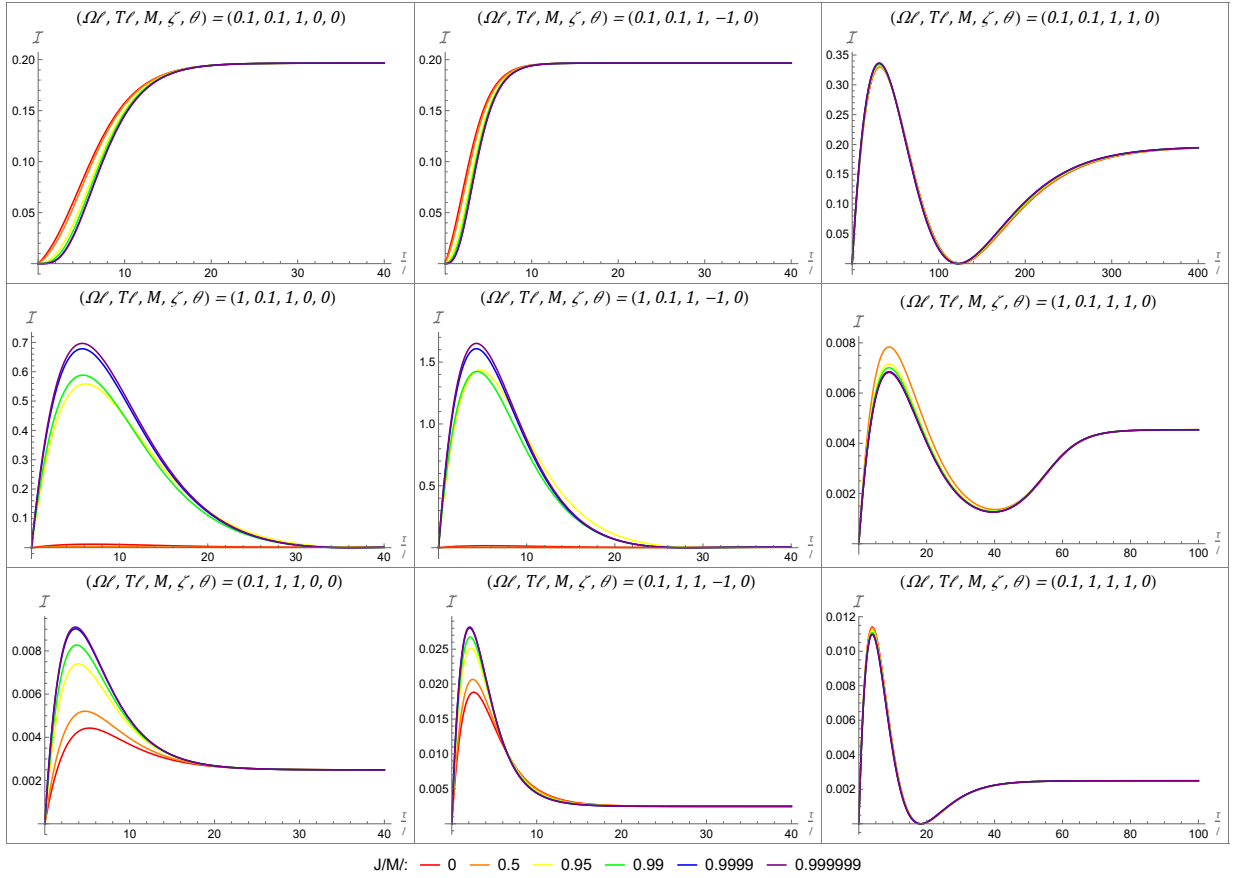
Figure 4.9: We examine the effect that a change in the angular momentum, J, has on the Fisher information. The colours of the rainbow correspond to increasing angular momentum ranging from the static case, to a near-extremal $J/M\ell = 0.999999$ case. Throughout the plot, the mass, M, and the initial state, θ, are fixed, while the boundary condition, ζ, is fixed in each column, and the ratio Ω/T is fixed in each row. We note that there is significant amplification of the Fisher information occurring in the 'cold' set up, except for the Dirichlet ($\zeta = 1$) boundary condition, where there a suppression effect instead. We further note that the Dirichlet boundary condition seems to have the opposite effect relative to the other boundary conditions when it comes to varying J, while there is almost no effect when $\Omega = T$.

of these is the reversal of the effect that increasing the angular momentum of the black hole has on the Fisher information. An increase in $J/M\ell$ may lead to an increase of the Fisher information for the transparent and Neumann boundary conditions, but leads to a

40

decrease in the Fisher information in the Dirichlet boundary condition, and vice versa.

If we instead turn our attention to the change in behaviour from row to row, corresponding to a change in the Ω/T ratio, we notice from the first row that when $\Omega = T$ the change in $J/M\ell$ leads to only a very minute variation in the Fisher information. This is somewhat reminiscent of the results from AdS and the static BTZ spacetimes in which a ratio of unity also led to the Fisher information being almost fixed under most variations.

On the other hand, when $\Omega \neq T$ we are treated to quite interesting results. In the 'cold' case (middle row of Figure 4.9), where $\Omega\ell = 1$ and $T\ell = 0.1$, we observe as much as a 60-fold increase in the Fisher information with transparent boundary conditions as a result of an increase in the angular momentum of the black hole. Most excitingly, while this behaviour appears to be monotonic, there is actually no increase (and even a slight decrease) from $J/M\ell = 0$ to $J/M\ell = 0.5$ with the most dramatic increase in the Fisher information arise between $J/M\ell = 0.5$ and $J/M\ell = 0.95$, followed by another smaller boost between $J/M\ell = 0.99$ and $J/M\ell = 0.9999$. This suggests that a moderate increase in the angular momentum reduces the Fisher information, though further increasing the angular momentum beyond $J/M\ell = 0.5$ leads to a dramatic increase in the Fisher information. This increase in the Fisher information is present for both the transparent and Neumann boundary conditions.

However, for the Dirichlet boundary conditions we actually see the opposite effect. When $\zeta = 1$, an increase in the angular momentum results in a (small) decrease of the maximal Fisher information!

When considering the 'hot' set up (bottom row of Figure 4.9), we see a similar behaviour, though the increase for the transparent and Neumann boundary conditions and the decrease for the Dirichlet boundary condition are indeed monotonic, though at most by a factor of two. This goes to show the relevance of both the energy gap to temperature ratio and the boundary condition when it comes to the relation between the black hole's angular momentum and the Fisher information. In particular, these parameters form the difference between the a greater angular momentum having no effect, an enhancing effect, or a suppressing effect.

If we now turn our attention to the effect of a variation in $J/M\ell$ for a small mass of $M = 0.01$, we notice from Figure 4.10 some very different behaviours. The most striking of these is that in the 'cold' set up, we observe the opposite trend from what had been seen for the $M = 1$ case: an increase in the angular momentum leads to a dramatic decrease in the Fisher information for the transparent and Neumann boundary conditions, but an increase for Dirichlet boundary conditions. In particular, the Fisher information can decrease by a whole order of magnitude for Neumann boundary conditions, while it increases by a factor
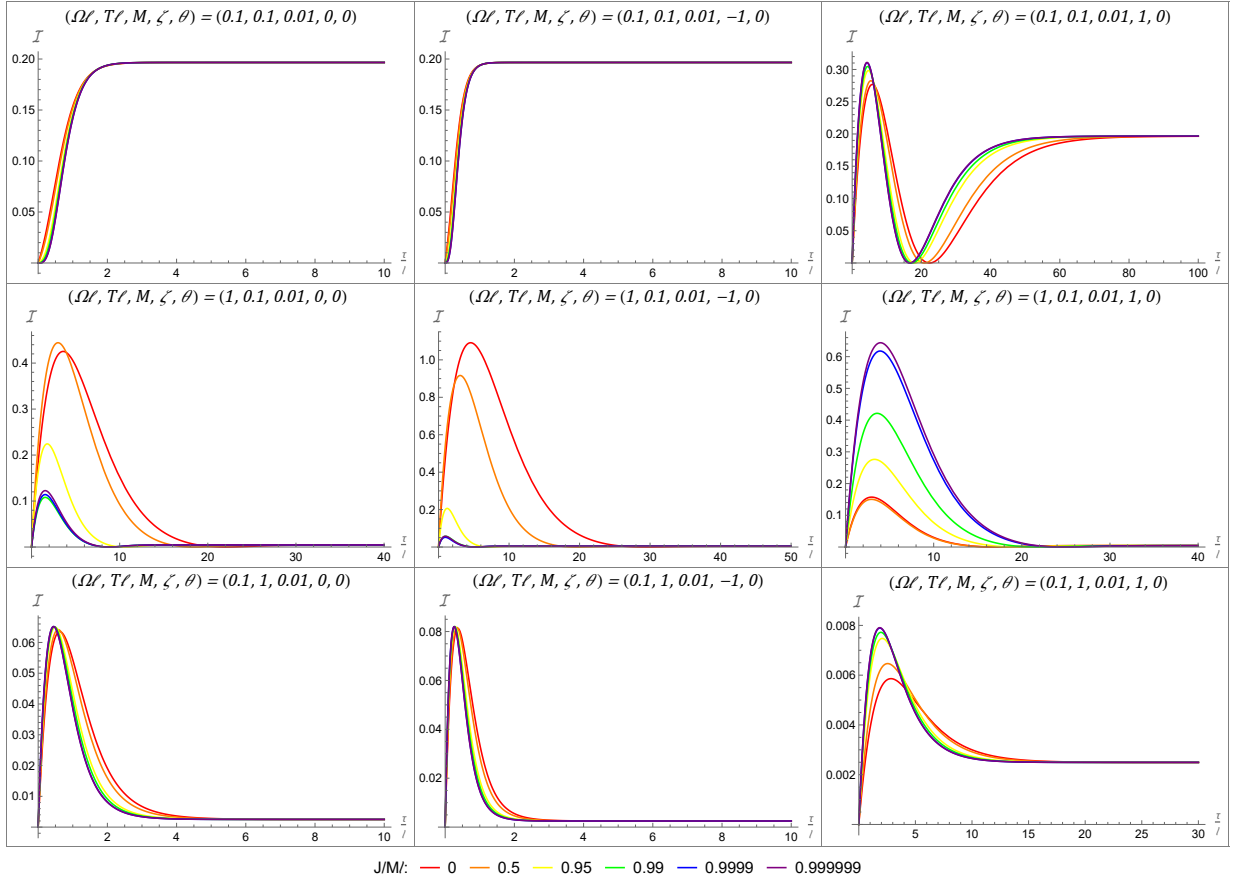
Figure 4.10: Here we depict the effect of varying the angular momentum, J, for a small BTZ mass of $M = 0.01$. While we retain some trends from the $M = 1$ case depicted in Figure 4.9, such as not much change when $\Omega = T$, and the Dirichlet ($\zeta = 1$) boundary condition having distinct behaviours compared to the other boundary condition, there are also some new effects. Most notably, for the 'cold' set up, the Fisher information is now suppressed for increasing angular momentum in the transparent ($\zeta = 0$) and Neumann ($\zeta = -1$) boundary condition, while there is a significant increase for the Dirichlet boundary condition.

of four for the Dirichlet boundary condition.

Interestingly, in the 'hot' set up for $M = 0.01$ (bottom row of Figure 4.10), we notice an ever so slight increase and shift of the Fisher information for increasing angular momentum. While this shift may appear more important for the Dirichlet boundary condition, we note that in this case the range of the Fisher information is so small that even small changes

appear significant. Here, the effect of the angular momentum seems to affect the Fisher information in a very similar fashion regardless of the boundary condition, more so than for any of the conditions for $M = 1$ outlined in Figure 4.9.

For $\Omega = T$ (top row of Figure 4.10), we see a very slight horizontal shift for the transparent and Neumann boundary conditions, suggesting that the Fisher information remains insensitive to rotation here. However, the Dirichlet boundary condition bucks the trend of the $\Omega = T$ cases being left unaffected by rotation. There is a clear (albeit not large) amplification effect.

While there remains an overall trend of the Dirichlet boundary condition leading to different effects than the transparent and Neumann boundary conditions, for $M = 0.01$ the similarities lie in the 'hot' set up rather than in the $\Omega = T$ set up like for $M = 1$. It is also worth noting that while the transparent and Neumann boundary conditions displayed the same qualitative behaviour with respect ot the varying angular momentum for $M = 1$ in Figure 4.9, in the 'cold' set up for $M = 0.01$, there is a slight increase in the Fisher information for the transparent boundary condition from $J/M\ell = 0$ to $J/M\ell = 0.5$ before the decreasing trend, while the Neumann boundary condition appears to decrease monotonically.

Overall, the most dramatic effect to be depicted in Figure 4.10 remains the significant amplification and suppression present for the 'cold' set-up. But what makes these results even more dramatic is that this is a full reversal of the behaviours relative to those for $M = 1$ depicted in Figure 4.9. This clearly points towards a more complex interplay between the variance in mass and the variance in the angular momentum.

In particular, it is not unreasonable to imagine that there exists some mass parameter between $M = 0.01$ and $M = 1$ for which there is neither amplification nor suppression of the Fisher information. Having said this, the fluctuations of the Fisher information with respect to mass are quite dramatic in this 'cold' set up, and $J/M\ell$ obviously has some dependence on M, so it might well be tricky to disentangle the two. We would certainly expect the presence of some oscillatory effect to arise from the mass variation, so it is not clear how this would overlap with the rotational effects seen here. Computing this will likely provide a challenge as it is the primarily the mass that dictates the number of terms required in the sum of Equation (3.25), but we separately require the mass in plotting the angular momentum effect. One should try to be clever in running the code to ensure convergence of the terms of interest, while not requiring too much computational effort.

Regardless, there are some clearly interesting behaviours of the Fisher that arise as a result of rotation in the BTZ spacetime. These are highly dependent on each of the mass, the Ω/T ratio, and the boundary condition at spatial infinity. It will be particularly

interesting to see how the mass and angular momentum interact in more detail, though this may take significant computational efforts.

Chapter 5

Conclusion

In this thesis, we set out to identify and describe the Fisher information of a black hole spacetime for the first time. In particular, we considered the thermal Fisher information from a UDW detector conformally coupled to a massless scalar field in 2+1 dimensions. We analysed the behaviour of the Fisher information with respect to time for AdS, BTZ, and rotating BTZ spacetimes in order to understand the effect of the black hole on this quantity. The motivation for this work was two-fold.

First, we sought to provide a better understanding of the Fisher information in black hole spacetimes in order to facilitate the implementation of optimal estimation strategies of the KMS temperature using quantum detectors. The thermalization of quantum detectors is an important feature of QFT in curved spacetime, with the (anti-) Hawking and (anti-) Unruh effects being examples of features that can be identified by a thermalized detector [50, 38, 25].

Second, we wanted to further see if the Fisher information could serve as a black hole probe by telling us something about the spacetime, based solely on the Fisher information. For all the recent advancements in our understanding of black holes, they remain a deeply mysterious object with profound implications for fundamental physics. As such, it is always helpful to have a new stick with which to prod them and the Fisher information offers a slightly different paradigm with which to consider the effects of black holes on the quantum vacuum.

We found that the presence of black holes resulted in significant changes to the Fisher information. The mere presence of a black hole enabled the identification of new Fisher information behaviours not observed until now. This provided us with the most clear-cut way to identify the presence of a black hole based on the Fisher information.

Having identified a discriminator between the BTZ black hole and AdS space, we were then able to turn our attention to the effect of mass on the Fisher information. We found that there is a very important effect that is most pronounced as the energy gap of the detector grows larger than the KMS temperature. This effect is an oscillatory effect that can either amplify or diminish the Fisher information depending on the mass of the black hole. Thus, we can identify the mass of the black hole from the Fisher information, given the other parameters of our system.

Lastly, while considering the rotating BTZ black hole, we found that the angular momentum led to both amplification and suppression of the Fisher information. This was most pronounced for near-extremal black holes. These consisted of both significant increases and decreases in the Fisher information depending on the mass and other parameters.

It should be noted that while we may not get to choose the black hole mass, angular momentum, or the boundary condition in an 'experimental' setting, we can conceivably have some say on the energy gap of our detector. Tuning this parameter, especially with respect to the KMS temperature, can significantly improve or worsen a given estimation protocol. We might gather even more information about our system by considering an array of detectors with various energy gaps from which we could cross-reference the behaviours.

With these first results about the Fisher information of black holes in hand, we can now consider what may be the next steps in this work.

Having found informative results about the Fisher information in black hole spacetimes, it would be interesting to further this line of inquiry by analysing the behaviour of the quantum Fisher information (QFI) [62]. This measure is known to better exploit the quantum nature of a physical system [22], offering not only the possibility of refining previous results, but also yielding novel insight into relativistic quantum interactions. Beyond the natural extension to our current results, QFI has been shown to be an effective tool for detecting curvature [63] and it may offer a new perspective into interesting properties of the BTZ black hole vacuum [50].

Otherwise, we might consider extending the analysis of the Fisher information to more physically relevant black hole spacetimes in 3+1 dimensions. These include the standard Schwarzschild and Kerr black holes along with constant curvature topological black holes [64, 65]. While the BTZ spacetime is frequently used as a first step in black hole spacetime analyses due to its simpler structure that preserves the key features of black holes, it is important to understand whether or not the novel results found in 2+1 dimensions are also present in 3+1 dimensions.

This Fisher information analysis of (2+1)-dimensional spacetimes, including a first such analysis of a black hole spacetimes, provides us with a better understanding of the Fisher

information, both as it pertains to RQM and parameter estimation and as a probe of the underlying spacetime. However, we hope that this thesis also serves as a stepping stone towards a better understanding of the quantum structure of black holes and spacetime on both the theoretical and experimental fronts.

References

[1] Everett Patterson and Robert B. Mann. Fisher information of a black hole spacetime, https://arxiv.org/abs/2207.12226.

[2] Robert M. Wald. General Relativity. University of Chicago Press, 1984.

[3] P.A. Tipler and R. Llewellyn. Modern Physics. W. H. Freeman, 2007.

[4] Tatsumi Aoyama, Masashi Hayakawa, Toichiro Kinoshita, and Makiko Nio. Tenth-order electron anomalous magnetic moment: Contribution of diagrams without closed lepton loops. Physical Review D, 91(3):033006, February 2015.

[5] Rainer Weiss. Nobel lecture: Ligo and the discovery of gravitational waves i. Rev. Mod. Phys., 90:040501, Dec 2018.

[6] Barry C. Barish. Nobel lecture: Ligo and gravitational waves ii. Rev. Mod. Phys., 90:040502, Dec 2018.

[7] Reinhard Genzel. Nobel lecture: A forty-year journey. Rev. Mod. Phys., 94:020501, Jun 2022.

[8] Event Horizon Telescope Collaboration. First M87 Event Horizon Telescope Results. I. The Shadow of the Supermassive Black Hole. The Astrophysical Journal Letters, 875(1):L1, April 2019.

[9] S Carlip. Quantum gravity: a progress report. Reports on Progress in Physics, 64(8):885–942, jul 2001.

[10] Katrin Becker, Melanie Becker, and John H. Schwarz. String Theory and M-Theory: A Modern Introduction. Cambridge University Press, 2006.

[11] Carlo Rovelli. Quantum Gravity. Cambridge Monographs on Mathematical Physics. Cambridge University Press, 2004.

[12] Robert B Mann and Timothy C Ralph. Relativistic quantum information. Classical and Quantum Gravity, 29(22):220301, 2012.

[13] Nicholas David Birrell and P.C.W. Davies. Quantum fields in curved space. Cambridge University Press, 1984.

[14] William G Unruh. Notes on black-hole evaporation. Physical Review D, 14(4):870, 1976.

[15] Bryce S DeWitt. Quantum gravity: the new synthesis. In Stephen Hawking and Werner Israel, editors, General relativity: An Einstein Centenary Survey, pages 680–745. Cambridge University Press, 1979.

[16] Matthew P G Robbins, Laura J Henderson, and Robert B Mann. Entanglement amplification from rotating black holes. Classical and Quantum Gravity, 39(2):02LT01, dec 2021.

[17] Allison Sachs, Robert B. Mann, and Eduardo Martí n-Martínez. Entanglement harvesting and divergences in quadratic Unruh-DeWitt detector pairs. Physical Review D, 96(8), oct 2017.

[18] Mehdi Ahmadi, David Edward Bruschi, and Ivette Fuentes. Quantum metrology for relativistic quantum fields. Phys. Rev. D, 89:065028, Mar 2014.

[19] Mehdi Ahmadi, David Edward Bruschi, Carlos Sabín, Gerardo Adesso, and Ivette Fuentes. Relativistic quantum metrology: Exploiting relativity to improve quantum measurement technologies. Scientific reports, 4:4996, 2014.

[20] Vittorio Giovannetti, Seth Lloyd, and Lorenzo Maccone. Advances in quantum metrology. Nature Photonics, 5, 2011.

[21] Samuel L. Braunstein and Carlton M. Caves. Statistical distance and the geometry of quantum states. Phys. Rev. Lett., 72:3439–3443, May 1994.

[22] Matteo GA Paris. Quantum estimation for quantum technology. International Journal of Quantum Information, 7(supp01):125–137, 2009.

[23] Xiaobin Zhao, Yuxiang Yang, and Giulio Chiribella. Quantum metrology with indefinite causal order. Phys. Rev. Lett., 124:190503, May 2020.

[24] Carlo Cepollaro, Flaminia Giacomini, and Matteo G. A. Paris. Gravitational time dilation as a resource in quantum sensing, 2022.

[25] Mariona Aspachs, Gerardo Adesso, and Ivette Fuentes. Optimal quantum estimation of the Unruh-Hawking effect. Phys. Rev. Lett., 105:151301, Oct 2010.

[26] Xiaoyang Huang, Jun Feng, Yao-Zhong Zhang, and Heng Fan. Quantum estimation in an expanding spacetime. Annals of Physics, 397:336–350, 2018.

[27] Magdalena Zych, Fabio Costa, Igor Pikovski, and Časlav Brukner. Quantum interferometric visibility as a witness of general relativistic proper time. Nature Communications, 2(1), sep 2011.

[28] Chin-Wen Chou, David Hume, J.C. Koelemeij, David Wineland, and Till Rosenband. Frequency comparison of two high-accuracy Al+ optical clocks. (104), 2010-02-17 2010.

[29] Zehua Tian, Jieci Wang, Jiliang Jing, and Andrzej Dragan. Entanglement enhanced thermometry in the detection of the Unruh effect. Annals of Physics, 377:1–9, 2017.

[30] Jan Kohlrus, David Edward Bruschi, Jorma Louko, and Ivette Fuentes. Quantum communications and quantum metrology in the spacetime of a rotating planet. EPJ Quantum Technology, 4.

[31] Haoxing Du and Robert B. Mann. Fisher information as a probe of spacetime structure: relativistic quantum metrology in (A)dS. Journal of High Energy Physics, 2021, 2021.

[32] The CHIME Collaboration. An Overview of CHIME, the Canadian Hydrogen Intensity Mapping Experiment. The Astrophysical Journal Supplement Series, 261(2):29, jul 2022.

[33] C Radhakrishna Rao. Information and the accuracy attainable in the estimation of statistical parameters. In Breakthroughs in statistics, pages 235–247. Springer, 1992.

[34] Harald Cramér. Mathematical methods of statistics, volume 43. Princeton university press, 1999.

[35] Laura Henderson. What can detectors detect? PhD Thesis, University of Waterloo, 2021.

[36] Laura J Henderson, Robie A Hennigar, Robert B Mann, Alexander R H Smith, and Jialin Zhang. Harvesting entanglement from the black hole vacuum. Classical and Quantum Gravity, 35(21):21LT02, oct 2018.

[37] W.G. Brenna, Robert B. Mann, and Eduardo Martín-Martínez. Anti-Unruh phenomena. Physics Letters B, 757:307–311, jun 2016.

[38] Luis J. Garay, Eduardo Martín-Martínez, and José de Ramón. Thermalization of particle detectors: The Unruh effect and its reverse. Physical Review D, 94(10), nov 2016.

[39] David Jennings. On the response of a particle detector in anti-de Sitter spacetime. Classical and Quantum Gravity, 27(20):205005, 2010.

[40] Jorma Louko and Alejandro Satz. Transition rate of the Unruh–DeWitt detector in curved spacetime. Classical and Quantum Gravity, 25(5):055012, 2008.

[41] Paul Langlois. Causal particle detectors and topology. Annals Phys., 321:2027–2070, 2006.

[42] Alexander R. H. Smith and Robert B. Mann. Looking Inside a Black Hole. Class. Quant. Grav., 31:082001, 2014.

[43] Eduardo Martin-Martinez, Alexander R. H. Smith, and Daniel R. Terno. Spacetime structure and vacuum entanglement. Phys. Rev. D, 93(4):044001, 2016.

[44] Finnian Gray, David Kubiznak, Taillte May, Sydney Timmerman, and Erickson Tjoa. Quantum imprints of gravitational shockwaves. JHEP, 11:054, 2021.

[45] Laura J. Henderson, Su Yu Ding, and Robert B. Mann. Entanglement harvesting with a twist. AVS Quantum Sci., 4(1):014402, 2022.

[46] Gary W Gibbons and Stephen W Hawking. Cosmological event horizons, thermodynamics, and particle creation. Physical Review D, 15(10):2738, 1977.

[47] Geoffrey L Sewell. Quantum fields on manifolds: Pct and gravitationally induced thermal states. Annals of Physics, 141(2):201–224, 1982.

[48] Stephen W Hawking. Particle creation by black holes. Communications in mathematical physics, 43(3):199–220, 1975.

[49] Stanley Deser and Orit Levin. Accelerated detectors and temperature in (anti-) de Sitter spaces. Classical and Quantum Gravity, 14(9):L163, 1997.

[50] Laura J Henderson, Robie A Hennigar, Robert B Mann, Alexander RH Smith, and Jialin Zhang. Anti-Hawking phenomena. Physics Letters B, 809:135732, 2020.

[51] S Carlip. The (2+1)-dimensional black hole. Classical and Quantum Gravity, 12(12):2853–2879, dec 1995.

[52] Lee Hodgkinson and Jorma Louko. Static, stationary, and inertial Unruh-DeWitt detectors on the BTZ black hole. Physical Review D, 86(6), sep 2012.

[53] Gilad Lifschytz and Miguel Ortiz. Scalar field quantization on the (2+1)-dimensional black hole background. Phys. Rev. D, 49:1929–1943, Feb 1994.

[54] Máximo Bañados, Claudio Teitelboim, and Jorge Zanelli. Black hole in three-dimensional spacetime. Physical Review Letters, 69(13):1849–1851, sep 1992.

[55] R. Kubo. Statistical-mechanical theory of irreversible processes. I. general theory and simple applications to magnetic and conduction problems. J. Phys. Soc. Jpn., 12:570, 1957.

[56] Paul C. Martin and Julian Schwinger. Theory of many-particle systems. I. Phys. Rev., 115:1342–1373, Sep 1959.

[57] Fabio Benatti and R Floreanini. Entanglement generation in uniformly accelerating atoms: Reexamination of the Unruh effect. Physical Review A, 70(1):012112, 2004.

[58] Zehua Tian, Jieci Wang, Heng Fan, and Jiliang Jing. Relativistic quantum metrology in open system dynamics. Scientific reports, 5(1):1–6, 2015.

[59] Daniel Manzano. A short introduction to the Lindblad master equation. AIP Advances, 10(2):025106, 2020.

[60] SJ Avis, CJ Isham, and D Storey. Quantum field theory in anti-de Sitter space-time. Physical Review D, 18(10):3565, 1978.

[61] Matthew P. G. Robbins and Robert B. Mann. Anti-Hawking phenomena around a rotating BTZ black hole. Phys. Rev. D, 106:045018, Aug 2022.

[62] Dénes Petz and Catalin Ghinea. Introduction to quantum Fisher information. In Quantum probability and related topics, pages 261–281. World Scientific, 2011.

[63] Daniele Bonalda, Luigi Seveso, and Matteo G. A. Paris. Quantum Sensing of Curvature. International Journal of Theoretical Physics, 58:2914–2935, 2019.

[64] Lissa de Souza Campos and Claudio Dappiaggi. Ground and thermal states for the Klein-Gordon field on a massless hyperbolic black hole with applications to the anti-Hawking effect. Phys. Rev. D, 103(2):025021, 2021.

[65] Lissa De Souza Campos. Probing thermal effects on static spacetimes with Unruh-DeWitt detectors. PhD Thesis, Pavia U., 2022.

[66] Milton Abramowitz and Irene A. Stegun. Handbook of Mathematical Functions with Formulas, Graphs, and Mathematical Tables. Dover, New York City, ninth Dover printing, tenth GPO printing edition, 1964.

[67] NIST Digital Library of Mathematical Functions. http://dlmf.nist.gov/, Release 1.1.8 of 2022-12-15. F. W. J. Olver, A. B. Olde Daalhuis, D. W. Lozier, B. I. Schneider, R. F. Boisvert, C. W. Clark, B. R. Miller, B. V. Saunders, H. S. Cohl, and M. A. McClain, eds.

APPENDICES

Appendix A

Detailed Derivation of Response Rates

In this appendix, we will present a more detailed derivation of the response rates described by Equations 3.8, 3.17, and 3.25.

A.1 Detailed Derivations in AdS

We will recall our formula for the response rate of a detector along a stationary trajectory to be

$$\mathcal{F}(\Omega) = \int_{-\infty}^{\infty} d\Delta\tau e^{-i\Omega\Delta\tau} W(\Delta\tau), \tag{A.1}$$

where $W(\Delta\tau)$ is the Wightman function for a stationary trajectory. In general, the Wightman function is given by

$$W_{\text{AdS}}(x, x') = \frac{1}{4\sqrt{2}\pi\ell} \left[\frac{1}{\sqrt{\sigma(x, x')}} - \frac{\zeta}{\sqrt{\sigma(x, x') + 2}} \right], \tag{A.2}$$

where $\sigma(x, x')$ is the squared geodesic distance

$$\sigma(x, x') = \frac{1}{2\ell^2} \left[(X_1 - X_1')^2 - (T_1 - T_1')^2 + (X_2 - X_2')^2 - (T_2 - T_2')^2 \right]. \tag{A.3}$$

We note that Subsections A.1.3 and A.1.4 were inspired by notes shared by L.J. Henderson addressing the work in [50].

A.1.1 Computing the squared distance

We can explicitly compute this squared geodesic distance in terms of our metric coordinates by applying the coordinate transforms mentioned previously. Doing so, we find that

$$
\begin{aligned}
(X_1 - X_1')^2 - (T_1 - T_1')^2 &= (r\sinh\phi - r'\sinh\phi')^2 - (r\cosh\phi - r'\cosh\phi')^2 \\
&= r^2\sinh^2\phi - 2rr'\sinh\phi\sinh\phi' + r'^2\sinh^2\phi' \\
&\quad - r^2\cosh^2\phi + 2rr'\cosh\phi\cosh\phi' - r'^2\cosh^2\phi' \\
&= -r^2(\cosh^2\phi - \sinh^2\phi) - r'^2(\cosh^2\phi' - \sinh^2\phi') \\
&\quad + 2rr'(\cosh\phi\cosh\phi' - \sinh\phi\sinh\phi') \\
&= -r^2 - r'^2 + 2rr'(\cosh\phi\cosh\phi' - \sinh\phi\sinh\phi') \\
&= -r^2 - r'^2 + 2rr'\cosh(\phi - \phi'), \quad\quad\quad\quad\quad\text{(A.4)}
\end{aligned}
$$

while

$$
\begin{aligned}
(X_2 - X_2')^2 - (T_2 - T_2')^2 &= + \left(\sqrt{r^2 - \ell^2}\cosh\frac{t}{\ell} - \sqrt{r'^2 - \ell^2}\cosh\frac{t'}{\ell}\right)^2 \\
&\quad - \left(\sqrt{r^2 - \ell^2}\sinh\frac{t}{\ell} - \sqrt{r'^2 - \ell^2}\sinh\frac{t'}{\ell}\right)^2 \\
&= (r^2 - \ell^2)\cosh^2\frac{t}{\ell} - 2\sqrt{(r^2 - \ell^2)(r'^2 - \ell^2)}\cosh\frac{t}{\ell}\cosh\frac{t'}{\ell} \\
&\quad + (r'^2 - \ell^2)\cosh^2\frac{t'}{\ell} - (r^2 - \ell^2)\sinh^2\frac{t}{\ell} \\
&\quad + 2\sqrt{(r^2 - \ell^2)(r'^2 - \ell^2)}\sinh\frac{t}{\ell}\sinh\frac{t'}{\ell} - (r'^2 - \ell^2)\sinh^2\frac{t'}{\ell} \\
&= (r^2 - \ell^2) + (r'^2 - \ell^2) \\
&\quad - 2\sqrt{(r^2 - \ell^2)(r'^2 - \ell^2)}\left(\cosh\frac{t}{\ell}\cosh\frac{t'}{\ell} - \sinh\frac{t}{\ell}\sinh\frac{t'}{\ell}\right) \\
&= r^2 + r'^2 - 2\ell^2 - 2\sqrt{(r^2 - \ell^2)(r'^2 - \ell^2)}\cosh\left(\frac{t - t'}{\ell}\right) \quad\text{(A.5)}
\end{aligned}
$$

So,

$$\begin{aligned}
\sigma(x,x') =& \frac{1}{2\ell^2}\left[(X_1 - X_1')^2 - (T_1 - T_1')^2 + (X_2 - X_2')^2 - (T_2 - T_2')^2\right]\\
=& \frac{1}{2\ell^2}\left[-r^2 - r'^2 + 2rr'\cosh(\phi - \phi')\right.\\
&\left. +r^2 + r'^2 - 2\ell^2 - 2\sqrt{(r^2-\ell^2)(r'^2-\ell^2)}\cosh\left(\frac{t-t'}{\ell}\right)\right]\\
=& \frac{1}{2\ell^2}\left[-2\ell^2 + 2rr'\cosh(\phi - \phi') - 2\sqrt{(r^2-\ell^2)(r'^2-\ell^2)}\cosh\left(\frac{t-t'}{\ell}\right)\right]\\
=& -1 + \frac{rr'}{\ell^2}\cosh(\Delta\phi) - \frac{\sqrt{(r^2-\ell^2)(r'^2-\ell^2)}}{\ell^2}\cosh\left(\frac{\Delta t}{\ell}\right) \quad\quad (A.6)
\end{aligned}$$

In AdS spacetime, we consider a detector travelling a constantly accelerating trajectory, or equivalently in AdS-Rindler coordinates, the detector would travel along a stationary trajectory. Recall that this trajectory, originally defined in Equation (3.1) is given by

$$x_D(\tau) := \left\{t = \frac{\tau}{\sqrt{f(R_D)}}, r = R_D, \phi = \Phi_D\right\}. \quad\quad (A.7)$$

The squared distance in AdS along this trajectory can thus be expressed as

$$\begin{aligned}
\sigma(x,x') &= -1 + \frac{R_D^2}{\ell^2}\cosh(0) - \frac{\sqrt{(R_D^2-\ell^2)(R_D^2-\ell^2)}}{\ell^2}\cosh\left(\frac{\Delta\tau}{\ell\sqrt{f(R_D)}}\right)\\
&= -1 + \frac{R_D^2}{\ell^2} - \frac{R_D^2 - \ell^2}{\ell^2}\cosh\left(\frac{\Delta\tau}{\ell\sqrt{f(R_D)}}\right)\\
&= \frac{R_D^2 - \ell^2}{\ell^2} - \frac{R_D^2 - \ell^2}{\ell^2}\cosh\left(\frac{\Delta\tau}{\ell\sqrt{f(R_D)}}\right)\\
&= \frac{R_D^2 - \ell^2}{\ell^2}\left[1 - \cosh\left(\frac{\Delta\tau}{\ell\sqrt{f(R_D)}}\right)\right]\\
&= f(R_D)\left[1 - \cosh\left(\frac{\Delta\tau}{\ell\sqrt{f(R_D)}}\right)\right]. \quad\quad (A.8)
\end{aligned}$$

Applying the hyperbolic double angle identity, we can rewrite $\sigma(x,x')$ as

$$\sigma(x,x') = -2f(R_D)\left[\sinh^2\left(\frac{\Delta\tau}{2\ell\sqrt{f(R_D)}}\right)\right] \quad\quad (A.9)$$

A.1.2 Computing the Wightman function

Turning our attention to the Wightman function, we can now write in terms of our AdS-Rindler coordinates by inserting the expression found for $\sigma(x, x')$ in Equation (A.9). Doing so, we have

$$
W_{\text{AdS}}(x, x') = \frac{1}{4\sqrt{2}\pi\ell} \left(\frac{1}{\sqrt{\sigma(x, x')}} - \frac{\zeta}{\sqrt{\sigma(x, x') + 2}} \right)
$$

$$
= \frac{1}{4\sqrt{2}\pi\ell} \left(\frac{1}{\sqrt{-2f(R_D)\sinh^2\left(\frac{\Delta\tau}{2\ell\sqrt{f(R_D)}}\right)}} - \frac{\zeta}{\sqrt{-2f(R_D)\sinh^2\left(\frac{\Delta\tau}{2\ell\sqrt{f(R_D)}}\right) + 2}} \right)
$$

$$
= \frac{1}{8\pi\ell\sqrt{f(R_D)}} \left(\frac{1}{\sqrt{-\sinh^2(\Delta\tau/(2\sqrt{f(R_D)}\ell))}} \right.
$$

$$
\left. - \frac{\zeta}{\sqrt{1/f(R_D) - \sinh^2(\Delta\tau/(2\sqrt{f(R_D)}\ell))}} \right). \tag{A.10}
$$

Rewriting the Wightman function in terms of the KMS temperature [50] by using

$$
\sqrt{f(R_D)} = \frac{1}{2\pi\ell T}, \tag{A.11}
$$

we obtain

$$
W_{\text{AdS}}(x, x') = \frac{2\pi\ell T}{8\pi\ell} \left(\frac{1}{\sqrt{-\sinh^2(\Delta\tau 2\pi\ell T/(2\ell))}} - \frac{\zeta}{\sqrt{4\pi^2\ell^2 T^2 - \sinh^2(\Delta\tau 2\pi\ell T/(2\ell))}} \right)
$$

$$
= \frac{T}{4} \left(\frac{1}{\sqrt{-\sinh^2(\Delta\tau\pi T)}} - \frac{\zeta}{\sqrt{4\pi^2\ell^2 T^2 - \sinh^2(\Delta\tau\pi T)}} \right). \tag{A.12}
$$

A.1.3 Response rate

The final, but also most involved step in our derivation will be to compute the response rate per se.

Substituting the Wightman function from Equation (A.12) into Equation (A.1), we obtain

$$\mathcal{F}_{\text{AdS}} = \frac{T}{4} \int_{-\infty}^{\infty} d\Delta\tau \, e^{-i\Omega\Delta\tau} \left(\frac{1}{\sqrt{-\sinh^2(\Delta\tau\pi T)}} - \frac{\zeta}{\sqrt{4\pi^2\ell^2 T^2 - \sinh^2(\Delta\tau\pi T)}} \right). \quad (A.13)$$

Let $z = \pi T \Delta\tau$, then $dz = \pi T d\Delta\tau$. We can thus rewrite response rate as

$$\mathcal{F}_{\text{AdS}} = \frac{1}{4\pi} \int_{-\infty}^{\infty} dz \, e^{\frac{-i\Omega z}{\pi T}} \left(\frac{1}{\sqrt{-\sinh^2(z)}} - \frac{\zeta}{\sqrt{4\pi^2\ell^2 T^2 - \sinh^2(z)}} \right), \quad (A.14)$$

We will now simplify the expressions following the integral sign by considering the two terms separately (with the second containing the boundary condition ζ).

To solve the first term, we first add a regulator in the denominator to avoid the branch cut

$$\mathcal{F}_{\text{AdS}}^{(1)} = \frac{1}{4\pi} \int_{-\infty}^{\infty} dz \, \frac{e^{\frac{-i\Omega z}{\pi T}}}{\sqrt{-\sinh^2(z - i\epsilon)}}. \quad (A.15)$$

There is a simple pole at $z = 0$, so it cannot be directly integrated. However one can show that $\sqrt{-\sinh^2(z - i\epsilon)} \approx i\sinh(z) + \epsilon, \quad \forall z$. Thus

$$\mathcal{F}_{\text{AdS}}^{(1)} = \frac{1}{4\pi} \frac{1}{i} \int_{-\infty}^{\infty} dz \, \frac{e^{\frac{-i\Omega z}{\pi T}}}{\sinh(z) - i\epsilon}. \quad (A.16)$$

Letting $h(z) = e^{\frac{-i\Omega z}{\pi T}}$ and $g(z) = \sinh(z)$, we can then invoke Sokhotski's theorem:

$$\lim_{\epsilon \to 0} \int_{-\infty}^{\infty} dz \, \frac{h(z)}{g(z) \pm i\epsilon} = \mp i\pi \int_{-\infty}^{\infty} dz \, h(z)\delta(g(z)) + \text{PV} \int_{-\infty}^{\infty} dz \, \frac{h(z)}{g(z)}. \quad (A.17)$$

Since $g(z) = \sinh(z)$ which has a zero at $z_1 = 0$, we have that

$$\delta(g(z)) = \sum_i \frac{\delta(z - z_i)}{|g'(z_i)|} = \frac{\delta(z)}{\cosh(0)} = \delta(z). \quad (A.18)$$

Thus,

$$
\begin{aligned}
\mathcal{F}_{\text{AdS}}^{(1)} &= \frac{-i}{4\pi} \left(i\pi \int_{-\infty}^{\infty} dz\, e^{\frac{-i\Omega z}{\pi T}} \delta(z) + \text{PV} \int_{-\infty}^{\infty} dz\, \frac{e^{\frac{-i\Omega z}{\pi T}}}{\sinh(z)} \right) \\
&= \frac{1}{4} e^0 - \frac{i}{4\pi} \text{PV} \int_{-\infty}^{\infty} dz\, \frac{e^{\frac{-i\Omega z}{\pi T}}}{\sinh(z)} \\
&= \frac{1}{4} - \frac{i}{4\pi} \text{PV} \int_{-\infty}^{\infty} dz\, \frac{e^{\frac{-i\Omega z}{\pi T}}}{\sinh(z)}.
\end{aligned}
\tag{A.19}
$$

Turning our attention to the second term, we have

$$
\mathcal{F}_{\text{AdS}}^{(2)} = \frac{-\zeta}{4\pi} \int_{-\infty}^{\infty} dz\, \frac{e^{\frac{-i\Omega z}{\pi T}}}{\sqrt{4\pi^2 \ell^2 T^2 - \sinh^2(z)}}.
\tag{A.20}
$$

To solve this one, we will invoke the hyperbolic double angle identity and rescale $z \to z/2$ in order to write it as

$$
\mathcal{F}_{\text{AdS}}^{(2)} = \frac{-\zeta}{4\sqrt{2}\pi} \int_{-\infty}^{\infty} dz\, \frac{e^{\frac{-i\Omega z}{2\pi T}}}{\sqrt{1 + 8\pi^2 \ell^2 T^2 - \cosh(z)}}.
\tag{A.21}
$$

Breaking this into parts, then substituting $z' = -z$, and finally making use of complex conjugates, we have that

$$
\begin{aligned}
\mathcal{F}_{\text{AdS}}^{(2)} &= \frac{-\zeta}{4\sqrt{2}\pi} \left[\int_{-\infty}^{0} dz\, \frac{e^{\frac{-i\Omega z}{2\pi T}}}{\sqrt{1 + 8\pi^2 \ell^2 T^2 - \cosh(z)}} + \int_{0}^{\infty} dz\, \frac{e^{\frac{-i\Omega z}{2\pi T}}}{\sqrt{1 + 8\pi^2 \ell^2 T^2 - \cosh(z)}} \right] \\
&= \frac{-\zeta}{4\sqrt{2}\pi} \left[-\int_{\infty}^{0} dz'\, \frac{e^{\frac{i\Omega z'}{2\pi T}}}{\sqrt{1 + 8\pi^2 \ell^2 T^2 - \cosh(-z')}} + \int_{0}^{\infty} dz\, \frac{e^{\frac{-i\Omega z}{2\pi T}}}{\sqrt{1 + 8\pi^2 \ell^2 T^2 - \cosh(z)}} \right] \\
&= \frac{-\zeta}{4\sqrt{2}\pi} \left[\int_{0}^{\infty} dz'\, \frac{e^{\frac{i\Omega z'}{2\pi T}}}{\sqrt{1 + 8\pi^2 \ell^2 T^2 - \cosh(z')}} + \int_{0}^{\infty} dz\, \frac{e^{\frac{-i\Omega z}{2\pi T}}}{\sqrt{1 + 8\pi^2 \ell^2 T^2 - \cosh(z)}} \right] \\
&= \frac{-\zeta}{4\sqrt{2}\pi} \left[\left(\int_{0}^{\infty} dz\, \frac{e^{\frac{-i\Omega z}{2\pi T}}}{\sqrt{1 + 8\pi^2 \ell^2 T^2 - \cosh(z)}} \right)^* + \int_{0}^{\infty} dz\, \frac{e^{\frac{-i\Omega z}{2\pi T}}}{\sqrt{1 + 8\pi^2 \ell^2 T^2 - \cosh(z)}} \right] \\
&= \frac{-\zeta}{2\sqrt{2}\pi} \text{Re} \left[\int_{0}^{\infty} dz\, \frac{e^{\frac{-i\Omega z}{2\pi T}}}{\sqrt{1 + 8\pi^2 \ell^2 T^2 - \cosh(z)}} \right]
\end{aligned}
\tag{A.22}
$$

60

Putting it all back together, we find that the response rate for our detector following a constantly accelerating trajectory in AdS is given by

$$\mathcal{F}_{\text{AdS}} = \frac{1}{4} - \frac{i}{4\pi}\text{PV}\int_{-\infty}^{\infty} dz \frac{e^{-i\Omega z/(\pi T)}}{\sinh z} - \frac{\zeta}{2\pi\sqrt{2}}\text{Re}\int_{0}^{\infty} dz \frac{e^{-i\Omega z/(2\pi T)}}{\sqrt{1 + 8\pi^2\ell^2 T^2 - \cosh z}}. \quad \text{(A.23)}$$

A.1.4 Performing the integrals

Computing the first integral by applying the Cauchy principle value, we find that

$$\begin{aligned}
\mathcal{F}_{\text{AdS}}^{(1)} &= \frac{1}{4} - \frac{i}{4\pi}\text{PV}\int_{-\infty}^{\infty} dz \frac{e^{-i\Omega z/(\pi T)}}{\sinh z} \\
&= \frac{1}{4} - \frac{i}{4\pi}\left[-i\pi\tanh\left(\frac{\pi(\Omega/(\pi T))}{2}\right)\right] \\
&= \frac{1}{4}\left[1 - \tanh\left(\frac{\Omega}{2T}\right)\right]
\end{aligned} \quad \text{(A.24)}$$

The second term must be expressed in terms of Legendre polynomials and is of the form

$$\mathcal{F}_{\text{AdS}}^{(2)} = \frac{\zeta}{4}\left[1 - \tanh\left(\frac{\Omega}{2T}\right)\right]P_{-\frac{1}{2}+\frac{i\Omega}{2\pi T}}(1 + 8\pi^2\ell^2 T^2). \quad \text{(A.25)}$$

Ultimately, we are left with

$$\mathcal{F}_{\text{AdS}} = \frac{1}{4}\left[1 - \tanh\left(\frac{\Omega}{2T}\right)\right] \times \left\{1 - \zeta P_{-\frac{1}{2}+\frac{i\Omega}{2\pi T}}\left(1 + 8\pi^2\ell^2 T^2\right)\right\}, \quad \text{(A.26)}$$

A.2 Derivations for BTZ spacetimes

Given the significant similarities between the AdS-Rindler and BTZ spacetimes, we are able to recover the results for our detector in BTZ spacetimes in much the same as was done in AdS.

More specifically, we need to account for the identification $\Gamma : \phi \to \phi + 2\pi$ and the image sum that arises from the Wightman function. Neither of these significantly alters the mathematics involved. In fact, while the BTZ cases are undoubtedly more tedious owing to their larger terms, the mathematics are actually more simple since we do not need to invoke Sokhotski's theorem.

Appendix B

Mathematica Code and Other Miscellaneous Materials

In this appendix, we will discuss a little bit about how we used Mathematica code to compute and plot many of the results in this thesis. First, we will highlight one operation performed by Mathematica when attempting to simplify our equations. Second, we will include some of our code to give flavour as to how this work was produced.

B.1 Legendre Polynomial to Hypergeometric Function

We noticed that when we employed the `FullSimplify` command in Mathematica, it converted our Legendre polynomials, `LegendreP`, into hypergeometric functions, `Hypergeometric2F1`, which are presumably more basic within the language, or easier to compute.

We found that both Abromowitz and Stegun [66] and the National Institute for Standards and Technology's (NIST) Digital Library of Mathematical Functions (DLMF) [67] had identities relating Legendre polynomials to hypergeometric functions.

In [66]'s Equation 22.5.49, found on p.779, we have that

$$P_n(x) = {}_2F_1\left(-n, n+1; 1; \frac{1-x}{2}\right). \tag{B.1}$$

When comparing the arguments of our input Legendre polynomial against the output of Mathematica's hypergeometric function, we find that this does indeed seem to be how Mathematica is performing the transformation.

A similar, more general identity is offered by [67]'s Section 14: Legendre and related functions' Equation 14.3.1

$$P_\nu^\mu(x) = \left(\frac{1+x}{1-x}\right)^{\frac{\mu}{2}} \mathbf{F}\left(\nu+1, -\nu; 1-\mu; \frac{1}{2} - \frac{1}{2}x\right), \tag{B.2}$$

where the Ferrer's function of the first kind, $\mathbf{F}$, appears to be the same as Mathematica and [66]'s $_2F_1$ hypergeometric function. However, we are restricting ourselves to the case in which the general order, μ, is zero.

To illustrate the value of this transformation in our code, consider the rotating BTZ case. Here, we noticed that simply computing the response rate followed by Mathematica's `FullSimplify` had a long time (likely due to all of the image sum terms requiring a conversion of the Legendre polynomials). So we considered hard coding these in terms of the hypergeometric function, simplifying the terms in the image sum as follows:

$$\exp\left(\frac{inr_-\Omega}{\ell T}\right)\left(P_{\Omega'}(\alpha_n^-) - \zeta P_{\Omega'}(\alpha_n^+)\right) \tag{B.3}$$

$$= \frac{1}{4}e^{-\frac{\Omega}{2T}}\operatorname{sech}\left(\frac{\Omega}{2T}\right)\left[2\cos\left(\frac{nr_-\Omega}{lT}\right)\left(_2F_1\left(-\Omega', 1+\Omega'; 1; -\left(4l^2\pi^2T^2+1\right)\sinh^2\left(\frac{n\pi r_+}{l}\right)\right)\right) \tag{B.4}$$

$$-\zeta\,_2F_1\left(-\Omega', 1-\Omega'; 1; \frac{1}{2}\left(1 - 4l^2\pi^2T^2 - \left(4l^2\pi^2T^2+1\right)\cosh\left(\frac{2n\pi r_+}{l}\right)\right)\right)\right] \tag{B.5}$$

where $\Omega' = -\frac{1}{2} + \frac{i\Omega}{2\pi T}$.

B.1.1 Hypergeometric function derivative

When computing the Fisher information, we find ourselves computing the derivative of the Legendre polynomial from the response rate. The form of these derivatives is messy and rather uninformative, whereas derivatives of the hypergeometric function are easier to comprehend.

If our hypergeometric function was only being differentiated with respect to the last term, then the derivative would be given by Equation 15.5.1 from [67]:

$$\frac{d}{dz}F(a,b;c;z) = \frac{ab}{c}F(a+1,b+1;c+1;z). \tag{B.6}$$

However, we are taking the derivative with respect to the KMS temperature which is found in the first, second, and last term of our hypergeometric function. Mathematica computes the more general derivative as:

$$\frac{d}{dx}F(f(x),g(x);1;h(x)) = f(x)g(x)h'(x)F(f(x),g(x);1;h(x)) \tag{B.7}$$

$$+ g'(x)F^{(0,1,0,0)}(f(x),g(x);1;h(x)) \tag{B.8}$$

$$+ f'(x)F^{(1,0,0,0)}(f(x),g(x);1;h(x)) \tag{B.9}$$

though we are not provided with analytic expressions for $F^{(1,0,0,0)}$ and $F^{(0,1,0,0)}$. We presume these are symmetric to some degree due to the symmetry of the hypergeometric function between the first two arguments.

B.2   Actual Mathematica Code

Below, we have include an instance of the actual code used in Mathematica for this project. All of the code included here is for the AdS case as it is the shortest and simplest, though the structure of the code is very similar for the BTZ cases.

B.2.1   Set-up

The first part of our code defines the response rate before performing the various operations required to obtain the Fisher information. We have included some of the original comments demonstrating that the outputs were initially displayed and compared. Since many of these outputs are quite long, we have since decided to suppress them. We have kept the comments to remind us what we might expect to receive as output given various modifications of the code.

```
AdS Set-up
```

We first define the response rate of our detector in (3-dimensional) AdS.

```
In[9]:= RRAdS[\[CapitalOmega]_] =
  1/4 (1 - Tanh[\[CapitalOmega]/(
     2 T)]) (1 - \[Zeta] LegendreP[-(1/2) + (I \[CapitalOmega])/(2 \[Pi] T),
      1 + 8 \[Pi]^2 l^2 T^2]);
```

The coefficients of the Kossakowski matrix are then given by:

```
In[10]:= KossAAdS = (RRAdS[\[CapitalOmega]] + RRAdS[-\[CapitalOmega]])/
    2; // FullSimplify
KossBAdS = (RRAdS[\[CapitalOmega]] - RRAdS[-\[CapitalOmega]])/
    2; // FullSimplify
KossCAdS = RRAdS[0] - KossAAdS; // FullSimplify
```

From this we can in turn compute what I will call the "Kossakowski ratio".
It is interesting to note that in all of our physical set ups, this value
is the same and equal to R=-Tan[\[CapitalOmega]/(2T)]:

```
In[13]:= RAdS = KossBAdS/KossAAdS; // FullSimplify
```

The third component of the Bloch vector of the detector's final state is
then given by:

```
In[14]:= (* FullSimplify runs fast and reduces this expression to a very
clean form \
(4->1 lines, courtesy of LegendreP->Hypergeometric2F1). *)
azAdS = -Exp[-KossAAdS \[Tau]] Cos[\[Theta]] -
   RAdS (1 - Exp[-KossAAdS \[Tau]])  // FullSimplify

Out[14]= Tanh[\[CapitalOmega]/(2 T)] -
 E^(1/4 \[Tau] (-1 + \[Zeta] Hypergeometric2F1[
       1/2 - (I \[CapitalOmega])/(2 \[Pi] T),
       1/2 + (I \[CapitalOmega])/(2 \[Pi] T),
       1, -4 l^2 \[Pi]^2 T^2])) (Cos[\[Theta]] + Tanh[\[CapitalOmega]/(2 T)])
```

From this, we can now determine the Fisher information (Scaled by T^2):

65

```
In[15]:= (* Applying FullSimplify to this is taking 30+ min to run when a_z
hasn't been simplified. Without this it was 25 lines long on my home monitor
at 100% magnification.
Update: With a_z simplified, it runs fast and produces 4 lines, and \
FullSimplify does almost nothing more, except run for 5 min. *)
FAdS = D[azAdS, T]^2/(1 - azAdS^2) T^2 ;
```

Finally, we define the boundary conditions where \[Zeta]=0,1,-1
corresponds to Transparent, Dirichlet, and Neumann boundary conditions
respectively:

```
In[16]:= \[Zeta]s = {0, 1, -1};
```

B.2.2   Plotting

Here, we have included the code used to generate Figure 4.1. We first "plot" all of the
sub-images, including the inset images, but we suppress their output. Then we compile
them all into a final grid plot, which we do make visible. This grid plot was then saved as
a pdf which was inserted into this document.

```
Subscript[AdS, 3] Grid Plot - 8 distinct qualitative behaviours

adsBehaviour1 =
 Plot[Evaluate[
   Re[FAdS /. {\[CapitalOmega] -> 2, T -> 0.5, \[Theta] -> \[Pi],
       l -> 1, \[Zeta] -> 0} & /@ \[Zeta]s]], {\[Tau], 0, 100},
  PlotRange -> {0, 0.5},
  AxesLabel -> {Style[\[Tau]/\[ScriptL], 16], Style[F, 16]},
  PlotStyle -> {Black}, TicksStyle -> Directive["Label", 12],
  PlotLabel ->
   Style["(\[CapitalOmega]\[ScriptL], T\[ScriptL], \[Theta]) = (2, \
0.5, \[Pi])", Italic, 18, Black, FontFamily -> "Cambria"],
  ImageSize -> 400]

adsBehaviour2 =
 Plot[Evaluate[
   Re[FAdS /. {\[CapitalOmega] -> 2, T -> 0.5, \[Theta] -> \[Pi]/2,
```

```
        l -> 1, \[Zeta] -> 0}]], {\[Tau], 0, 100},
   PlotRange -> {0, 0.5},
   AxesLabel -> {Style[\[Tau]/\[ScriptL], 16], Style[F, 16]},
   PlotStyle -> {Black}, TicksStyle -> Directive["Label", 12],
   PlotLabel ->
    Style["(\[CapitalOmega]\[ScriptL], T\[ScriptL], \[Theta]) = (2, \
0.5, \[Pi]/2)", Italic, 18, Black, FontFamily -> "Cambria"],
   ImageSize -> 400]

adsBehaviour3 =
 Plot[Evaluate[
    Re[FAdS /. {\[CapitalOmega] -> 0.1, T -> 0.2, \[Theta] -> \[Pi],
       l -> 1, \[Zeta] -> 1}]], {\[Tau], 0, 200},
   PlotRange -> {0, 0.5},
   AxesLabel -> {Style[\[Tau]/\[ScriptL], 16], Style[F, 16]},
   PlotStyle -> {
RGBColor[0.08, 0.43, 0.85]}, TicksStyle -> Directive["Label", 12],
   PlotLabel ->
    Style["(\[CapitalOmega]\[ScriptL], T\[ScriptL], \[Theta]) = (0.1, \
0.2, \[Pi])", Italic, 18, Black, FontFamily -> "Cambria"],
   ImageSize -> 400]

adsBehaviour4Inset =
 Plot[Evaluate[
    Re[FAdS /. {\[CapitalOmega] -> 0.01, T -> 0.2, \[Theta] -> \[Pi],
       l -> 1, \[Zeta] -> 1}]], {\[Tau], 50, 200},
   PlotRange -> {0, 0.01}, Frame -> True, PlotStyle -> {
RGBColor[0.08, 0.43, 0.85]}, TicksStyle -> Directive["Label", 8],
   ImageSize ->
    250]; (* Would be nice to reduce the number of ticks along the \
axes, just to remove some of the clutter *)

adsBehaviour4PlusInset =
  Plot[Evaluate[
     Re[FAdS /. {\[CapitalOmega] -> 0.01, T -> 0.2, \[Theta] -> \[Pi],
        l -> 1, \[Zeta] -> 1}]], {\[Tau], 0, 200},
    PlotRange -> {0, 0.5},
    AxesLabel -> {Style[\[Tau]/\[ScriptL], 16], Style[F, 16]},
```

```
    PlotStyle -> {
RGBColor[0.08, 0.43, 0.85]}, TicksStyle -> Directive["Label", 12],
    PlotLabel ->
     Style["(\[CapitalOmega]\[ScriptL], T\[ScriptL], \[Theta]) = \
(0.01, 0.2, \[Pi])", Italic, 18, Black, FontFamily -> "Cambria"],
    ImageSize -> 400,
    Epilog -> Inset[adsBehaviour4Inset, {133, 0.33}]];

(* No need to load. Kept for posterity *)
adsBehaviour4 =
  Plot[Evaluate[
    Re[FAdS /. {\[CapitalOmega] -> 0.01, T -> 0.2, \[Theta] -> \[Pi],
       l -> 1, \[Zeta] -> 1}]], {\[Tau], 0, 200},
   PlotRange -> {0, 0.5},
   AxesLabel -> {Style[\[Tau]/\[ScriptL], 16], Style[F, 16]},
   PlotStyle -> {
RGBColor[0.08, 0.43, 0.85]}, TicksStyle -> Directive["Label", 12],
   PlotLabel ->
    Style["(\[CapitalOmega]\[ScriptL], T\[ScriptL], \[Theta]) = \
(0.01, 0.2, \[Pi])", Italic, 18, Black, FontFamily -> "Cambria"],
   ImageSize ->
    400]; (*n note: this is the fake behaviour; actually the same as \
3 *)

adsBehaviour5 =
  Plot[Evaluate[
    Re[FAdS /. {\[CapitalOmega] -> 0.2, T -> 0.2, \[Theta] -> 0,
       l -> 1, \[Zeta] -> 1}]], {\[Tau], 0, 200},
   PlotRange -> {0, 0.5},
   AxesLabel -> {Style[\[Tau]/\[ScriptL], 16], Style[F, 16]},
   PlotStyle -> {
RGBColor[0.08, 0.43, 0.85]}, TicksStyle -> Directive["Label", 12],
   PlotLabel ->
    Style["(\[CapitalOmega]\[ScriptL], T\[ScriptL], \[Theta]) = (0.2, \
0.2, 0)", Italic, 18, Black, FontFamily -> "Cambria"],
   ImageSize -> 400];

adsBehaviour6Inset =
```

```
 Plot[Evaluate[
   Re[FAdS /. {\[CapitalOmega] -> 0.1, T -> 0.2, \[Theta] -> 0,
     l -> 1, \[Zeta] -> 1}]], {\[Tau], 51, 52.5},
  PlotRange -> {-0.00001, 0.00005}, Frame -> True, PlotStyle -> {
RGBColor[0.08, 0.43, 0.85]}, TicksStyle -> Directive["Label", 8],
  ImageSize -> 250];

adsBehaviour6PlusInset =
 Plot[Evaluate[
   Re[FAdS /. {\[CapitalOmega] -> 0.1, T -> 0.2, \[Theta] -> 0,
     l -> 1, \[Zeta] -> 1}]], {\[Tau], 0, 200},
  PlotRange -> {0, 0.5},
  AxesLabel -> {Style[\[Tau]/\[ScriptL], 16], Style[F, 16]},
  PlotStyle -> {
RGBColor[0.08, 0.43, 0.85]}, TicksStyle -> Directive["Label", 12],
  PlotLabel ->
   Style["(\[CapitalOmega]\[ScriptL], T\[ScriptL], \[Theta]) = (0.1, \
0.2, 0)", Italic, 18, Black, FontFamily -> "Cambria"],
  ImageSize -> 400,
  Epilog -> Inset[adsBehaviour6Inset, {133, 0.33}]];

adsBehaviour6 =
 Plot[Evaluate[
   Re[FAdS /. {\[CapitalOmega] -> 0.1, T -> 0.2, \[Theta] -> 0,
     l -> 1, \[Zeta] -> 1}]], {\[Tau], 0, 200},
  PlotRange -> {0, 0.5},
  AxesLabel -> {Style[\[Tau]/\[ScriptL], 16], Style[F, 16]},
  PlotStyle -> {
RGBColor[0.08, 0.43, 0.85]}, TicksStyle -> Directive["Label", 12],
  PlotLabel ->
   Style["(\[CapitalOmega]\[ScriptL], T\[ScriptL], \[Theta]) = (0.1, \
0.2, 0)", Italic, 18, Black, FontFamily -> "Cambria"],
  ImageSize -> 400];

adsBehaviour7 =
 Plot[Evaluate[
   Re[FAdS /. {\[CapitalOmega] -> 1, T -> 0.16, \[Theta] -> 0,
     l -> 1, \[Zeta] -> 1}]], {\[Tau], 0, 100},
```

```
    PlotRange -> {0, 0.1},
    AxesLabel -> {Style[\[Tau]/\[ScriptL], 16], Style[F, 16]},
    PlotStyle -> {
RGBColor[0.08, 0.43, 0.85]}, TicksStyle -> Directive["Label", 12],
   PlotLabel ->
    Style["(\[CapitalOmega]\[ScriptL], T\[ScriptL], \[Theta]) = (1, \
0.16, 0)", Italic, 18, Black, FontFamily -> "Cambria"],
   ImageSize -> 400];

adsBehaviour8 =
  Plot[Evaluate[
    Re[FAdS /. {\[CapitalOmega] -> 1.4, T -> 0.2, \[Theta] -> \[Pi]/2,
       l -> 1, \[Zeta] -> 1}]], {\[Tau], 0, 100},
   PlotRange -> {0, 0.05},
   AxesLabel -> {Style[\[Tau]/\[ScriptL], 16], Style[F, 16]},
   PlotStyle -> {
RGBColor[0.08, 0.43, 0.85]}, TicksStyle -> Directive["Label", 12],
   PlotLabel ->
    Style["(\[CapitalOmega]\[ScriptL], T\[ScriptL], \[Theta]) = (1.4, \
0.2, \[Pi]/2)", Italic, 18, Black, FontFamily -> "Cambria"],
   ImageSize -> 400];

adsBehaviour9 =
  Plot[Evaluate[
    Re[FAdS /. {\[CapitalOmega] -> 1.5, T -> 0.2, \[Theta] -> 0,
       l -> 1, \[Zeta] -> 1}]], {\[Tau], 0, 100},
   PlotRange -> {0, 0.06},
   AxesLabel -> {Style[\[Tau]/\[ScriptL], 16], Style[F, 16]},
   PlotStyle -> {
RGBColor[0.08, 0.43, 0.85]}, TicksStyle -> Directive["Label", 12],
   PlotLabel ->
    Style["(\[CapitalOmega]\[ScriptL], T\[ScriptL], \[Theta]) = (1.5, \
0.2, 0)", Italic, 18, Black, FontFamily -> "Cambria"],
   ImageSize -> 400];

adsGridPlotQualBehaviour =
 Legended[Grid[{{adsBehaviour1, adsBehaviour2,
     adsBehaviour3}, {adsBehaviour4PlusInset, adsBehaviour5,
```

```
    adsBehaviour6PlusInset}, {adsBehaviour7, adsBehaviour8,
    adsBehaviour9}}, Frame -> All, FrameStyle -> Gray],
Placed[LineLegend[{Black, RGBColor[0.08, 0.43, 0.85], RGBColor[
    0.9400000000000001, 0.25, 0.19]}, {"Transparent", "Dirichlet",
    "Neumann"},
  LegendLabel ->
   Placed[Style["Boundary condition:", Black, 16], Left],
  LabelStyle -> 16, LegendLayout -> "Row"], Bottom]]
```